Ph.D. Thesis

Measurements of time-dependent CP asymmetries in $B^0 \to D^*\pi$ decays using a full reconstruction technique

($B^0 \to D^*\pi$ 崩壊モードを用いたCP対称性の破れの測定)

Department of Physics, Tohoku University

Kennosuke Itagaki

平成26年

Abstract

We report the measurement of CP violation in $B^0(\overline{B}^0) \to D^{*\mp}\pi^{\pm}$ decays, using fully reconstruction technique. There are two ways that initial B^0 goes to a final state $D^{*-}\pi^+$. One is a Cabbibo-favoured decay (CFD) $\bar{b} \to \bar{c}u\bar{d}$ and the other is B^0 to $\overline{B}^0$ mixing followed by doubly-Cabbibo-suppressed decay (DCSD) $b \to u\bar{c}d$. Former does not have weak phase while later has phase of $2\phi_1 + \phi_3$ from mixing and decay. An interference between two decay paths causes CP violation and it can be measured from time dependent analysis. We measured CP violating parameters $S^{\pm}$ as

$$S^+ = 0.000 \pm 0.017(stat) \pm 0.011(sys) \quad (1)$$

$$S^- = 0.057 \pm 0.017(stat) \pm 0.011(sys) \quad (2)$$

Complete data set of 710 fb^{-1} accumulated by the Belle is used for this measurement.

Contents

Chapter 1

Introduction

1.1 The Standard Model

The Standard Model (SM) describes almost all the experimental results with no contradiction. The SM is a gauge theory with fermions which have four flavors. Four flavors are up-type quark, down-type quark, neutrino and charged lepton. There are three generations for each flavor. A kind of particle has a counterpart as anti-particle which has opposite charge from original particle. There are three gauge interaction $SU(3)\times SU(2)\times U_Y(1)$.

Fermions roughly consist of two types of particle. One is a quark and another is a lepton. Quarks don't exist independently. They can be found the component of hadrons. There are two types of hadron. One is a baryon which is composed of three quarks or anti-quarks, for example, proton(uud), neutron(udd). Another is a meson which composed of a quark and anti-quark, for example, $\pi^+(u\bar{d})$, $K^+(u\bar{s})$. Leptons, in contrast to quarks, can be observed as free particles. Every interaction has its own mediator as a boson. Gluon mediate the strong force. Photons mediate the electromagnetic force. $W^{\pm}$ and Z^0 bosons mediate the weak force. In addition, a higgs boson is needed in the SM to give the mass to the particles. The construction of the SM except Higgs are shown in Figure.1.1.

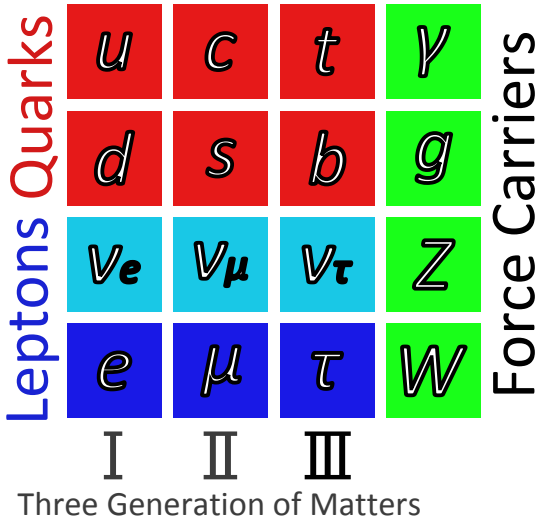

Figure 1.1: Construction of the standard model except Higgs.

1.2 CP violation and KM mechanism

Why the universe is made mostly of the matter and why there is very little anti-matter are the important questions for modern particle physics. According to the big bang theory the matter and the anti-matter are generated in equal proportions at the beginning of the universe. However, the world around us is dominated by the matter. The CP violation explains this state, as described by A. D. Sakharov [1].

In 1973, M.Kobayashi and T.Maskawa indicated that CP violation can occur within the SM framework if there are at least three quark generations. In their model, CP violation arises from a single irreducible complex phase in the Cabibbo-Kobayashi-Maskawa (CKM) quark mixing matrix [2][3], represented as:

$$V_{CKM} = \begin{pmatrix} V_{ud} & V_{us} & V_{ub} \\ V_{cd} & V_{cs} & V_{cb} \\ V_{td} & V_{ts} & V_{tb} \end{pmatrix}. \tag{1.1}$$

A matrix element V_{ij} represents the coupling constant through the charged current between a quark i and j.

If the number of quark family is three or more, there remain irreducible complex phase(s) that cannot be removed by choosing quark phases.

1.3 The Unitary Triangle

The matrix V_{CKM} is required to be unitary:

$$V_{CKM}^{\dagger} V_{CKM} = 1. \tag{1.2}$$

The Wolfenstein parametrization [4] is useful approximation in comparing the sizes of the matrix elements:

$$V_{CKM} = \begin{pmatrix} 1-\frac{1}{2}\lambda^2 & \lambda & A\lambda^3(\rho - i\eta) \\ -\lambda & 1-\frac{1}{2}\lambda^2 & A\lambda^2 \\ A\lambda^3(1-\rho-i\eta) & -A\lambda^2 & 1 \end{pmatrix} + \mathcal{O}(\lambda^4) \tag{1.3}$$

where A, ρ and η are real numbers whose order is unity. In this parametrization, quark phases are taken such that only V_{ub} and V_{td} have significant complex phases. Hereafter, we adopt this phase convention. λ is defined as

$$\lambda \equiv \sin\theta_c \simeq 0.22 \tag{1.4}$$

where θ_c is Cabbibo angle. From Eq.(1.4) $\lambda^2 \ll 1$, then the diagonal elements $\simeq 1$. On the other hand, the elements except diagonal elements are $\mathcal{O}(\lambda)$, $\mathcal{O}(\lambda^2)$ and $\mathcal{O}(\lambda^3)$. Therefore V_{CKM} is close to identity matrix.

Eq.(1.2) led to the following expression:

$$\sum_j V_{ij}^* V_{jk} = 0 \quad (i \neq k). \tag{1.5}$$

Since a sum of three complex quantities is zero, a triangle is drawn in complex plane by each of the equations. This triangle is called unitary triangle. The area of triangle has to be non-zero to establish CP violation. The most commonly used unitary triangle is obtained from:

$$V_{ub}^* V_{ud} + V_{cb}^* V_{cd} + V_{tb}^* V_{td} = 0. \tag{1.6}$$

The reason is that the magnitudes of three terms are all $\mathcal{O}(\lambda^3)$. As shown in Figure.1.2, all angles have some extent which can be measured. The angles of this triangle are represented as:

$$\phi_1 \equiv arg\left(\frac{V_{cd}V_{cb}^*}{-V_{td}V_{tb}^*}\right) \tag{1.7}$$

$$\phi_2 \equiv arg\left(\frac{V_{td}V_{tb}^*}{-V_{ud}V_{ub}^*}\right) \tag{1.8}$$

$$\phi_3 \equiv arg\left(\frac{V_{ud}V_{ub}^*}{-V_{cd}V_{cb}^*}\right). \tag{1.9}$$

Since these phases are fundamental parameters of the standard model, it is important to determine them. The measurement of ϕ_1 is already quite precise. Even though many different methods are carried out to measure ϕ_2 and ϕ_3, however, they are still limited by experimental and theoretical uncertainties.

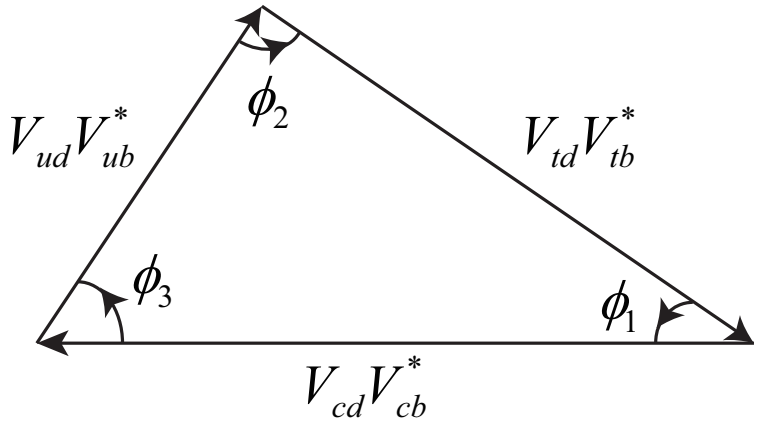

Figure 1.2: The unitary triangle of the CKM matrix.

SM is the successful theory. However, there are still some unsolved problems, fine tuning, unification of force, etc. The properties of the unitary triangle are hypothesized on the assumption that SM is established. If there were new physics, we observed inconsistency with a hypothesis by precise measurement. Polygonization by new flavor or inconsistency during some measurements can be estimated.

1.4 Motivation for $B^0(\overline{B}^0) \to D^{*\mp}\pi^{\pm}$ analysis

The neutral B-meson decay, $B^0(\overline{B}^0) \to D^{*\mp}\pi^{\pm}$ provides a sensitivity to $\sin(2\phi_1 + \phi_3)$ [7][8]. There are two ways that initial B^0 goes to a final state $D^{*-}\pi^+$. One is a Cabbibo-

favored decay (CFD) $\bar{b}\to\bar{c}u\bar{d}$ and another is B^0 to $\overline{B}^0$ mixing followed by doubly-Cabbibo-suppressed decay (DCSD) $b\to u\bar{c}d$ as shown in figure 1.3. The decay amplitude of CFD is proportional to the CKM matrix-elements $V_{cb}V_{ud}^*$. The decay amplitude of DCSD is proportional to the CKM matrix-elements $V_{cd}V_{ub}^*$. In our phase convention, former does not have CKM phase while later has phase of $2\phi_1+\phi_3$ from mixing and decay.

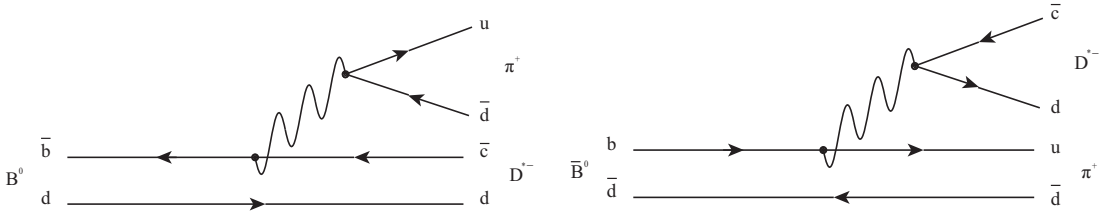

(a) $B^0\to D^{*-}\pi^+$ (CFD) (b) $\overline{B}^0\to D^{*-}\pi^+$ (DCSD)

Figure 1.3: Diagrams for $B^0(\overline{B}^0)\to D^{*-}\pi^+$

At KEK B factory, B mesons produced by the decay, $\Upsilon(4s)\to B\overline{B}$. We defined Δt as the difference between the decay time of B^0 and $\overline{B}^0$. If it identified clearly that $D^{*\mp}\pi^\pm$ were decayed from either B^0 or $\overline{B}^0$, the probability density functions were described as:

$$P(B^0\to D^{*-}\pi^+) = \frac{e^{-\frac{|\Delta t|}{\tau_{B^0}}}}{8\tau_{B^0}}[1+C\cos(\Delta m\Delta t)-S^-\sin(\Delta m\Delta t)] \quad (1.10)$$

$$P(B^0\to D^{*+}\pi^-) = \frac{e^{-\frac{|\Delta t|}{\tau_{B^0}}}}{8\tau_{B^0}}[1-C\cos(\Delta m\Delta t)-S^+\sin(\Delta m\Delta t)] \quad (1.11)$$

$$P(\overline{B^0}\to D^{*+}\pi^-) = \frac{e^{-\frac{|\Delta t|}{\tau_{B^0}}}}{8\tau_{B^0}}[1+C\cos(\Delta m\Delta t)+S^+\sin(\Delta m\Delta t)]. \quad (1.12)$$

$$P(\overline{B^0}\to D^{*-}\pi^+) = \frac{e^{-\frac{|\Delta t|}{\tau_{B^0}}}}{8\tau_{B^0}}[1-C\cos(\Delta m\Delta t)+S^-\sin(\Delta m\Delta t)]. \quad (1.13)$$

where τ_{B^0} is the lifetime of the neutral B meson, Δm is the $B^0-\overline{B}^0$ mixing frequency and $C=(1-R^2)/(1+R^2)$. R is the ratio between DCSD and CFD magnitudes, and about 0.02. $S^\pm$ are CP violating parameters described as:

$$S^+ = -\frac{2R}{1+R^2}\sin(2\phi_1+\phi_3+\delta) \quad (1.14)$$

$$S^- = -\frac{2R}{1+R^2}\sin(2\phi_1+\phi_3-\delta) \quad (1.15)$$

where δ is the strong phase difference between DCSD and CFD amplitudes. We extracted $S^\pm$ by this analysis. The difference between the probability density function of B^0 and $\overline{B^0}$ is described as:

$$A(\Delta t) = \frac{P(B^0\to D^{*\mp}\pi^\pm) - P(\overline{B^0}\to D^{*\pm}\pi^\mp)}{P(B^0\to D^{*\mp}\pi^\pm) + P(\overline{B^0}\to D^{*\pm}\pi^\mp)} = -\frac{S^+ + S^-}{2}\sin(\Delta m\Delta t) \quad (1.16)$$

where

$$P(B^0 \to D^{*\mp}\pi^{\pm}) = P(B^0 \to D^{*-}\pi^{+}) + P(B^0 \to D^{*+}\pi^{-}) \tag{1.17}$$
$$P(\overline{B^0} \to D^{*\pm}\pi^{\mp}) = P(\overline{B^0} \to D^{*+}\pi^{-}) + P(\overline{B^0} \to D^{*-}\pi^{+}). \tag{1.18}$$

We called $A(\Delta t)$ a asymmetry distribution. The amplitude is the average of S^+ and S^-.

We identified the B flavor by the tag-side B. Tag-side B is one of the $B^0(\overline{B}^0)$ from $\Upsilon(4S)$, which have not decayed to $D^{*\pm}\pi^{\mp}$. We mistake B^0 as $\overline{B}^0$ by a certain probability. We defined the wrong tag fraction as the probability to mistake. The probability density functions including the wrong tag fraction are described as:

$$P_{sig}(q = -1; B_{sig} \to D^{*\mp}\pi^{\pm}) = (1 - w_{\overline{B^0}})P(B^0 \to D^{*\mp}\pi^{\pm}) + w_{B^0}P(\overline{B^0} \to D^{*\mp}\pi^{\pm}) \tag{1.19}$$

$$P_{sig}(q = +1; B_{sig} \to D^{*\pm}\pi^{\mp}) = (1 - w_{B^0})P(\overline{B^0} \to D^{*\pm}\pi^{\mp}) + w_{\overline{B^0}}P(B^0 \to D^{*\pm}\pi^{\mp}). \tag{1.20}$$

We express the flavor of tag-side B by q. If q is 1, tag-side B is B^0. If q is -1, tag-side B is $\overline{B}^0$. The wrong tag fractions are described as $w_{\overline{B^0}}$ and w_{B^0}. We explain flavor tag in Chapter 3. Using eq.(1.19) and eq.(1.20), $A(\Delta t)$ becomes:

$$A(\Delta t) = (\Delta w - (1 - 2w)\frac{S^+ + S^-}{2})\sin(\Delta m \Delta t) \tag{1.21}$$

where

$$\Delta w \equiv w_{B^0} - w_{\overline{B^0}} \tag{1.22}$$
$$w \equiv \frac{w_{B^0} + w_{\overline{B^0}}}{2} \tag{1.23}$$

If the wrong tag fractions of B^0 and $\overline{B}^0$ were same, Δw became zero and $A(\Delta t)$ was diluted with $(1 - 2w)$ from eq.(1.16).

This decay has been studied by both the Belle and the BaBar. The BaBar introduced the following notations:

$$a = \frac{2R}{1 + R^2}\sin(2\phi_1 + \phi_3)\cos\delta \tag{1.24}$$
$$c = \frac{2R}{1 + R^2}\cos(2\phi_1 + \phi_3)\sin\delta \tag{1.25}$$

We can express a, c by $S^{\pm}$:

$$a = -\frac{S^+ + S^-}{2} \tag{1.26}$$
$$c = -\frac{S^+ - S^-}{2}. \tag{1.27}$$

As you can see, a is the amplitude of the asymmetry distribution. The strong phase difference are expressed by c. If δ equaled zero, c also equaled zero. The summary of the results for parameters, a and c from the previous the Belle and the BaBar are shown in figure.1.4

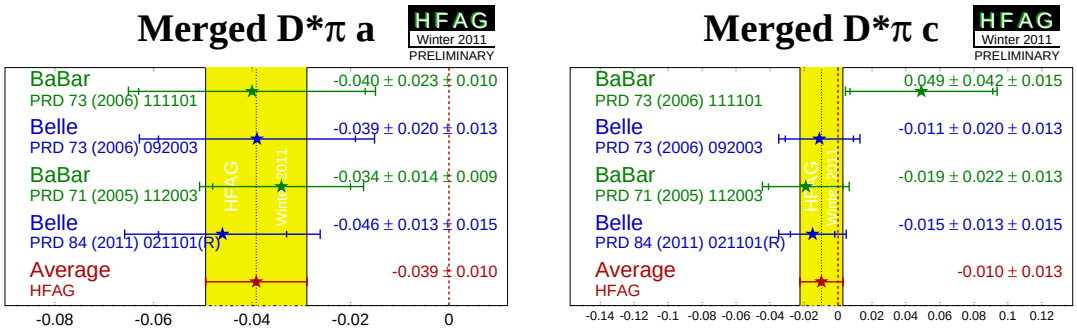

(a) a parameter (b) c parameter

Figure 1.4: previous results of the Belle and the Babar

Chapter 2

The Belle experiments using KEK B factory

2.1 Overview

The data set using this analysis is collected with KEK B factory. KEK B factory consists of two structures, KEKB accelerator[9] and the Belle detector[10]. They are located at the High Energy Accelerator Research Organization (KEK) in Tsukuba, Japan. In this chapter, we describe both of them.

The conventional definitions of the coordinates in the Belle experiments are as follows.

- x : horizontal direction, outward to KEKB accelerator
- y : vertical direction, upward.
- z : direction of the electron beam.
- r : $\sqrt{x^2 + y^2}$.
- θ : the polar angle with respect to z axis.
- φ : the azimuthal angle around z axis.

2.2 KEKB accelerator

KEKB accelerator is designed to produced a large number of B mesons via the interaction of $e^+e^- \to \Upsilon(4s) \to B\overline{B}$. It consists of two storage rings, a ring for 8 GeV electron and a ring for 3.5 GeV positron, they are called high energy ring (HER) and low energy ring (LER) respectively, and an injection linear accelerator. The two rings are side by side in the underground tunnel used for TRISTAN. The circumference is about 3 km. The length of the injection accelerator is about 600 m. The crossing point of two ring is located at one of the straight section of the ring. It is called the interaction point (IP). To separate e^+e^- beam after collision, e^+e^- crossing angle at IP is designed 22 mrad. The purpose to separate is for reducing backgrounds. Figure 2.1 shows the construction of KEKB.

To produce B mesons, the center-of-mass energy is set at:

$$\sqrt{s} \;=\; 2\times\sqrt{E_{HER}\cdot E_{LER}} \;=\; 10.58\,(GeV) \tag{2.1}$$

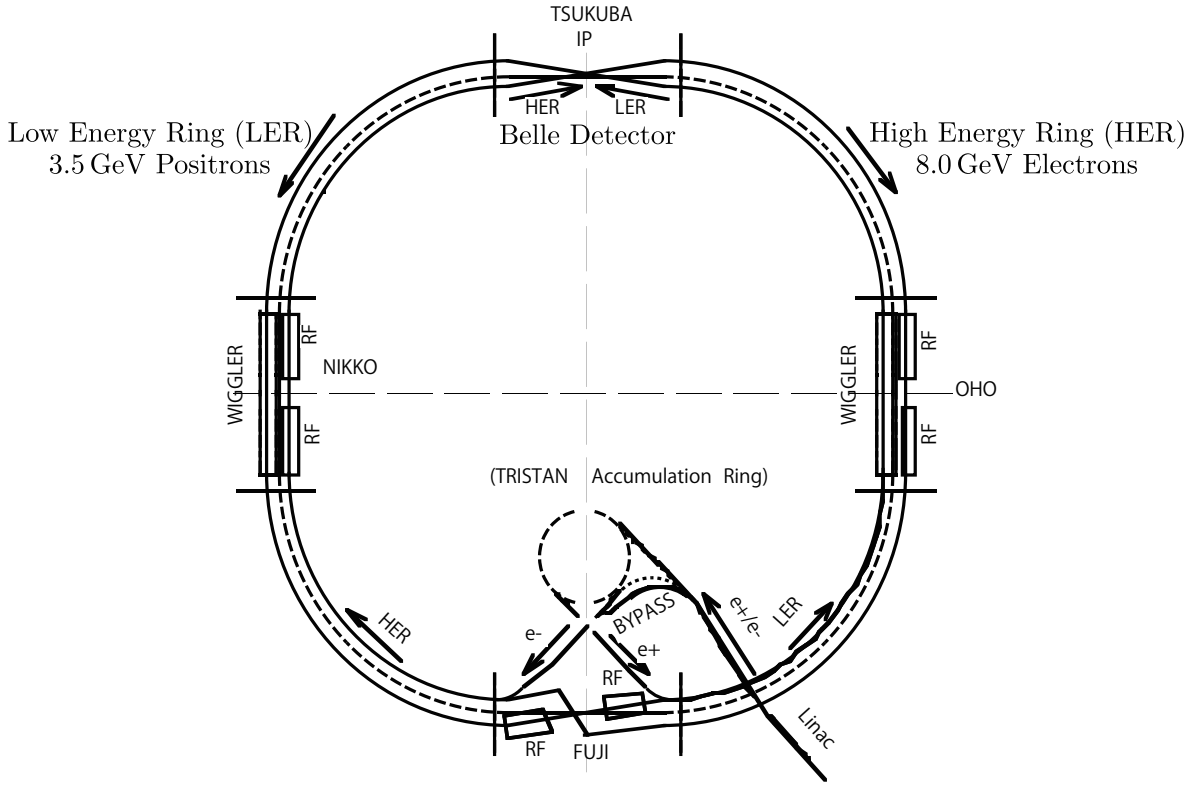

Figure 2.1: The configuration of KEKB accelerator.

which corresponds to the mass of $\Upsilon(4s)$ resonance. If above expression consists, we can choose any energies for the beam. One of the most important studies in the Belle experiments is the measurement of time dependent CP asymmetry. It needs to measure the difference between the decay times of $B^0\overline{B^0}$ pair. Unfortunately the lifetime of B meson is too short to measure directly. Then we generate B mesons with Lorentz boost according to z axis and measure the decay vertices of B mesons instead of decay times. The difference between the decay times (Δt) can be represented by the difference between the decay vertices (Δz) as:

$$\Delta t \simeq \frac{\Delta z}{c\beta\gamma}. \tag{2.2}$$

For this purpose, KEKB has an asymmetric energy as 8 GeV for e^- and 3.5 GeV for e^+. The Lorentz boost factor is:

$$\beta\gamma \;=\; \frac{E_{HER} - E_{LER}}{\sqrt{s}} \;=\; 0.425 \tag{2.3}$$

The typical B^0 meson decay length is:

$$l \;=\; c\beta\gamma\tau_{B^0} \simeq 200\,(\mu m). \tag{2.4}$$

The design luminosity of the KEKB accelerator is:

$$L \;=\; 1.0{\times}10^{34}\, cm^{-2}s^{-1} \tag{2.5}$$

which corresponds to an approximate production rate of 10 $B\overline{B}$ pairs per second. In June 2009, the world's highest luminosity of $L = 2.11\times10^{34}\,cm^{-2}s^{-1}$ was achieved, and the total integrated luminosity is reached to 1000 fb^{-1}. The KEKB luminosity histories are shown in Figure 2.2 and Figure 2.3

2.3 the Belle Detector

The Belle detector is a large solid-angle magnetic spectrometer that consists of many sub-detectors:

- Silicon Vertex Detector (SVD)
- Central Drift Chamber (CDC)
- Aerogel Cherenkov Counter (ACC)
- Time of Flight Counter (TOF)
- Electromagnetic Calorimeter (ECL)
- K_L and Muon Detector (KLM).

They are located inside a superconducting solenoid coil that provides a 1.5 T magnetic field without KLM. KLM is located outside the coil. Figure 2.4 and Figure 2.5 shows overhead view and section view of the Belle detector, respectively.

The purpose of the Belle detector is catch the B meson. B meson almost always will ultimately decay to some combination of following final state particles:

$$K^{\pm},\ \pi^{\pm},\ e^{\pm},\ p^{\pm},\ \mu^{\pm},\ \gamma,\ K^0_L.$$

Then it is important that these particles can be detected and identified with high efficiency. For time dependent analysis, the measurement of vertex position is also important. It needs that a track of a particle is reconstructed separately. The sub-detectors used for measurement of each particle are summarized in Table2.1.

Table 2.1: The measurement of the sub-detectors.

Particle	Position	Momentum	Energy	Particle Identification
$K^{\pm}$	SVD, CDC	CDC	ECL	ECL, ACC, TOF, CDC
$\pi^{\pm}$	SVD, CDC	CDC	×	ACC, TOF, CDC, KLM
$e^{\pm}$	SVD, CDC	CDC	×	ACC, TOF, CDC
$p^{\pm}$	SVD, CDC	CDC	×	ACC, TOF, CDC
$\mu^{\pm}$	SVD, CDC	CDC	×	ACC, TOF, CDC
γ	ECL	×	ECL	ECL, CDC
K^0_L	KLM	×	×	CDC, KLM

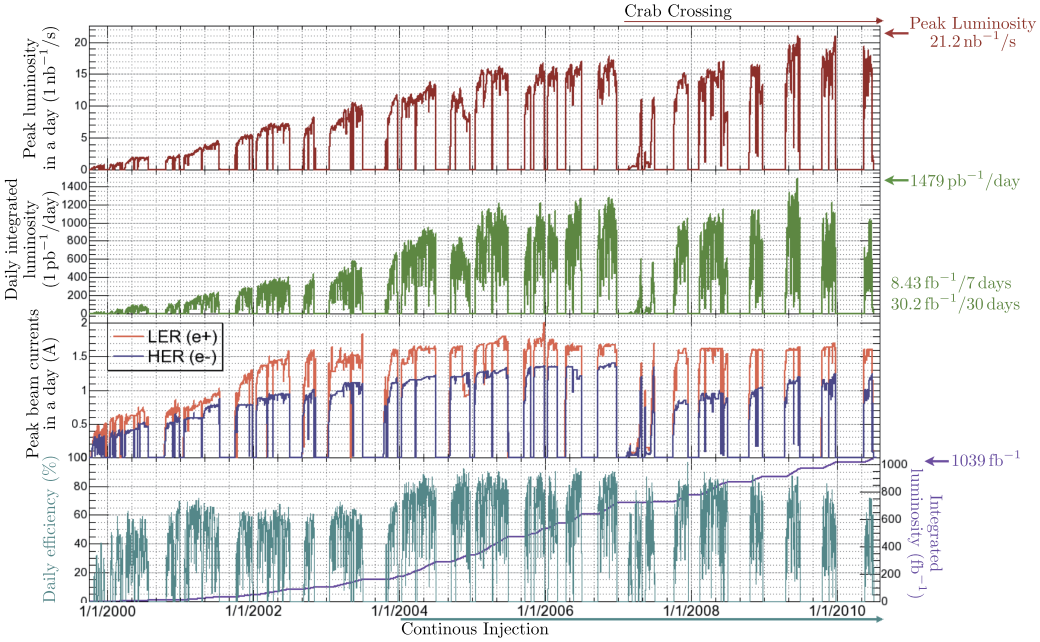

Figure 2.2: The luminosity history of KEKB accelerator.

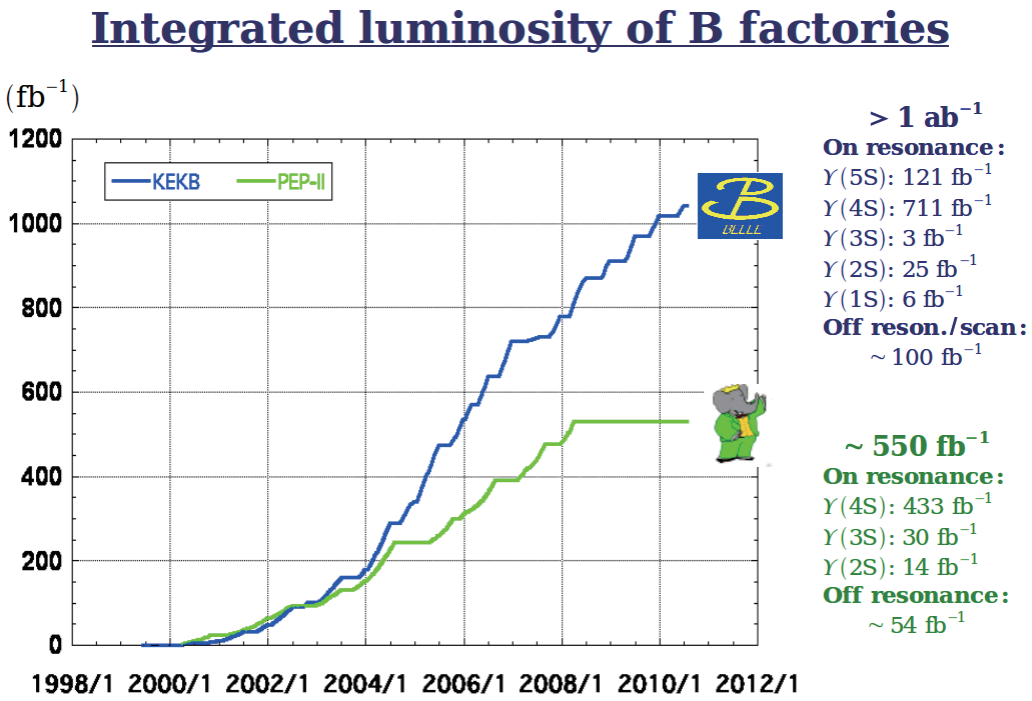

Figure 2.3: The integrated luminosity of the B factories, the Belle and the BABAR.

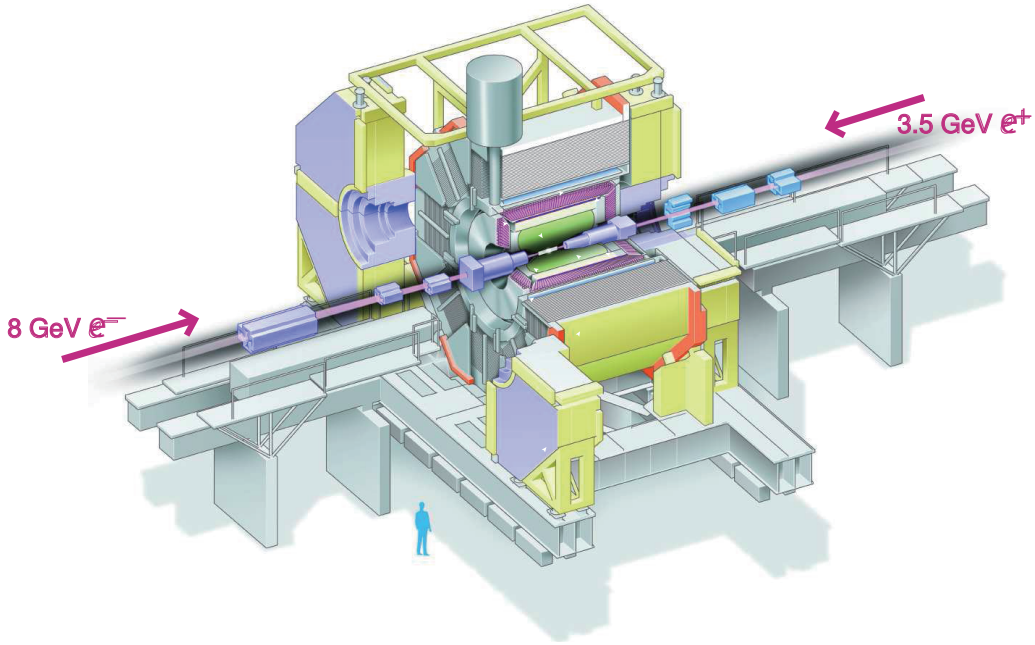

Figure 2.4: KEKB luminosity history.

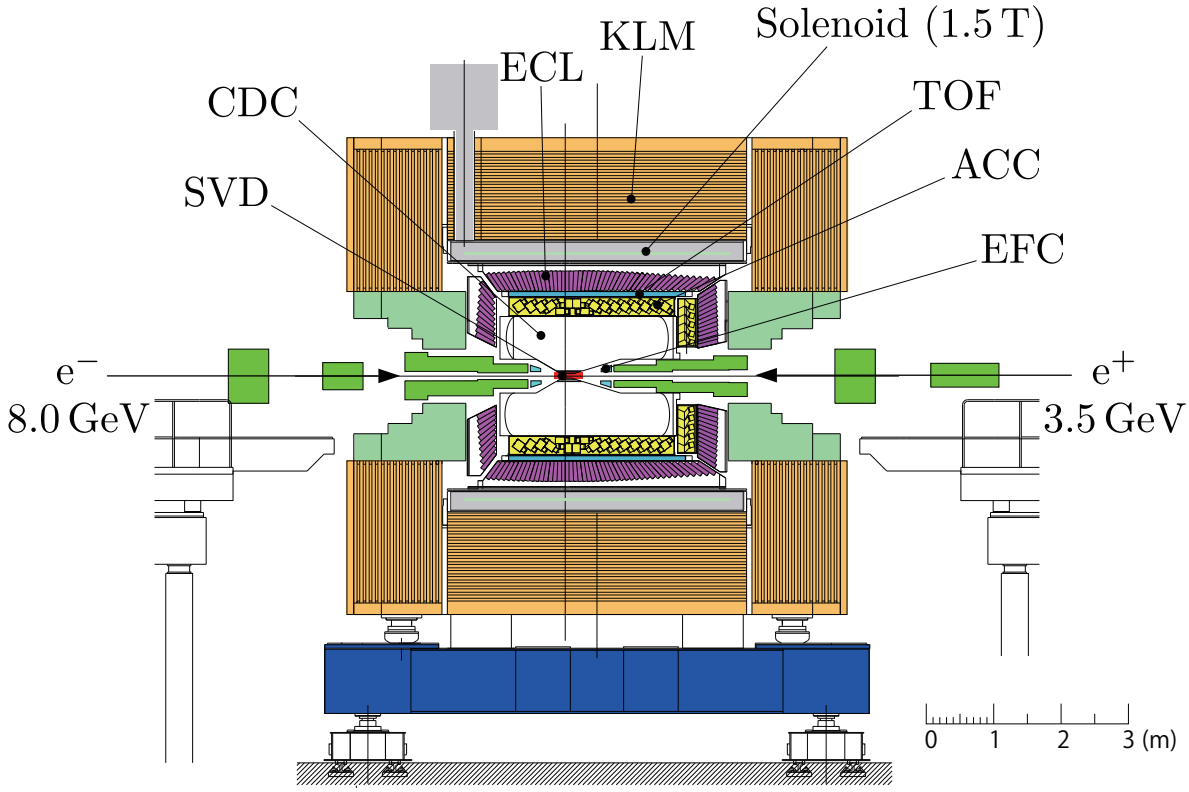

Figure 2.5: KEKB luminosity history.

Brief descriptions of each sub-detector are given in the following subsections.

2.3.1 Silicon Vertex Detector (SVD)

The Silicon Vertex Detector (SVD) [11] is the one of the most important detector in the Belle, because it provides a precise measurement of the B meson decay vertices. It is essential in the study of time-dependent CP asymmetry. For a time-dependent CP analysis, the z-separation between B vertices must be measured with a precision of about $100\,\mu$m. In addition, it is also used to measure the decay vertices of other particles. SVD was upgraded at the summer of 2003. We call the one before upgraded as SVD1 and the one after upgraded as SVD2 [12].

Figure 2.6 shows the side and the end views of the SVD1. It is the innermost detector and consists of three concentric layers of double-sided silicon strip detectors (DSSDs) and covers the polar angle range $23^\circ \leq \theta \leq 139^\circ$ where θ is the angle from the beam axis. This corresponds to 86% of the full solid angle. The radii of the innermost, middle, and outermost layers are 30.0 mm, 45.5 mm and 60.5 mm, respectively. The layers are constructed from 8, 10 and 14 independent ladders from inside to outside. Each ladder is made up of two half-ladders that are joined by a support structure but are electrically independent of each other. There are two kinds of half ladder, long half-ladder and short half ladder. A long half-ladder contains two DSSD and a CMOS-integrated circuit which processes signals from the DSSD. A short half-ladder contains a DSSD and a CMOS-integrated circuit. The innermost layers consist of two short half-ladders, the middle layers consist of a short and a long half-ladder and the outermost layers consist of two long half-ladders. Each DSSD size is $57.5\times33.5\,\mathrm{mm}^2$ and thickness is $300\,\mu$m. Each DSSD consists of 1280 sense strips and 640 readout pads on both sides. One side of the DSSD (called n-side) has its n^+ sense strips. They are oriented perpendicular to the beam direction to measure the z coordinate and separated by $42\,\mu$m. The p^+ sense strips, each separated by $25\,\mu$m, are oriented longitudinally to measure the $r-\varphi$ position. A DSSD is basically a p-n junction. When a charged particle passes through the DSSDs, it produces electron-hole pairs along its trajectory. The charges are then collected at the sense strips by the applied electric field. The charge distributions on the orthogonally segmented strips allow one to determine three-dimensional hit positions and hence, to reconstruct the particle track. The impact parameters of a reconstructed track are defined as the $r-\varphi$ and z distances of the closest approach of the track to the interaction point. The impact parameter resolution $\sigma_{r\varphi}$ and σ_z measured using cosmic rays events are shown in Figure 2.7 and well represented by the following E:

$$\sigma_{r\varphi} = 19.2 \oplus \frac{54.0}{p\beta\sin^{3/2}\theta}\ [\mu\mathrm{m}] \tag{2.6}$$

$$\sigma_z = 42.2 \oplus \frac{44.3}{p\beta\sin^{5/2}\theta}\ [\mu\mathrm{m}]. \tag{2.7}$$

SVD2 also consists DSSD, however, there are many improvements from SVD1. SVD2 consists of four concentric layers and covers the polar angle range $17^\circ \leq \theta \leq 150^\circ$. The radii of layers are 20.0 mm, 43.5 mm, 70.0 mm and 88.0 mm, and numbers of ladder are 6, 12, 18 and 18 from inside to outside. Figure 2.6 shows the SVD2. There are two kinds of DSSDs. One is used for inner three layers and has a size of $28.4\times79.6\,\mathrm{mm}^2$ with a strip pitch of $75\,\mu$m on the p-side and $50\,\mu$m on the n-side. For 4th layer, the size is

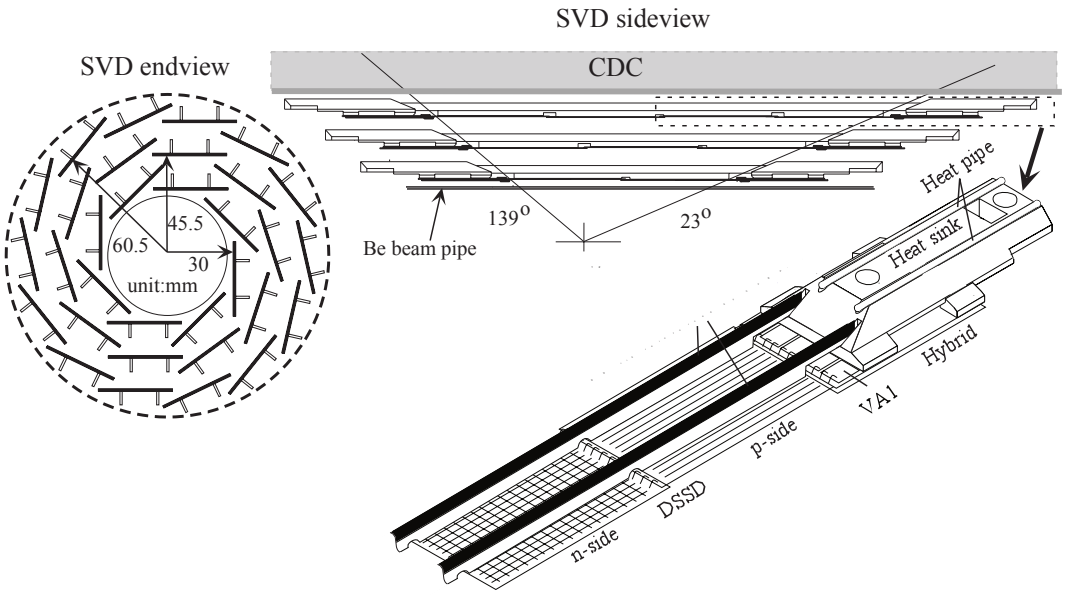

Figure 2.6: Configuration of SVD1.

$34.9 \times 76.4\,\mathrm{mm}^2$ with a strip pitch of $73\,\mu$m on the p-side and $65\,\mu$m on the n-side. The impact parameter resolutions are shown in Figure 2.7 and as follows:

$$\sigma_{r\varphi} = 21.9 \oplus \frac{35.5}{p\beta\sin^{3/2}\theta}\ [\mu\mathrm{m}] \tag{2.8}$$

$$\sigma_z = 27.8 \oplus \frac{31.9}{p\beta\sin^{5/2}\theta}\ [\mu\mathrm{m}]. \tag{2.9}$$

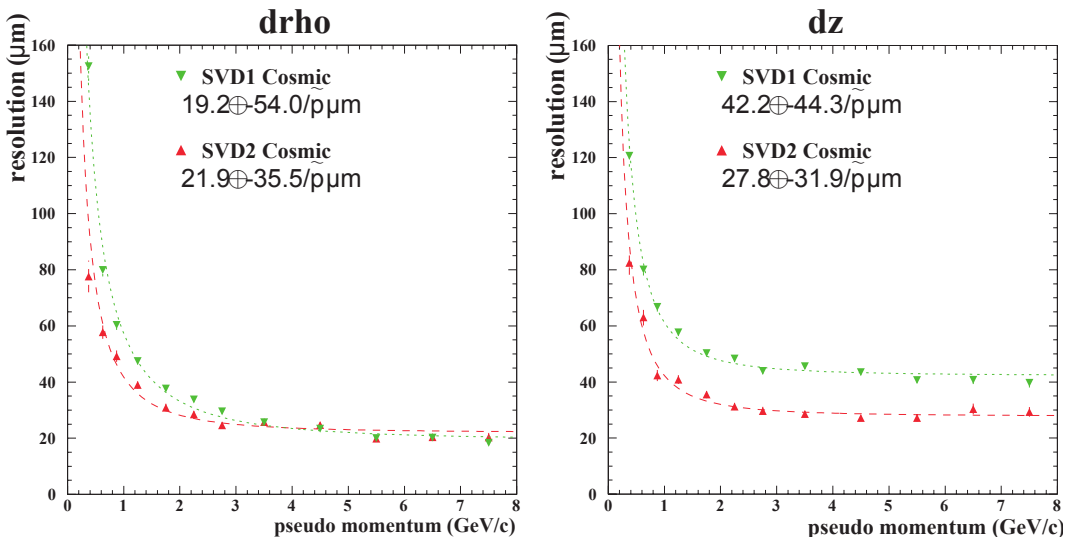

Figure 2.7: Impact parameter resolution of charged tracks with associated SVD hits from cosmic ray data. In the left plot, $\tilde{p} \equiv p\beta \sin^{3/2}\theta$, and in the right plot, $\tilde{p} \equiv p\beta \sin^{5/2}\theta$.

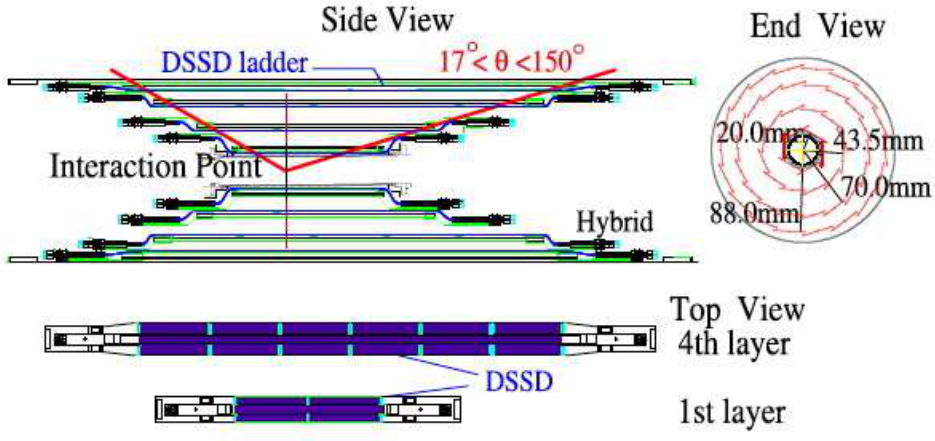

Figure 2.8: Configuration of SVD2.

2.3.2 Central Drift Chamber (CDC)

The Central Drift Chamber (CDC) [13] has been designed for efficient reconstruction of charged particle tracks and precise determination of their momenta. the Belle detector is in the uniform magnetic field induced by the solenoid magnet, the momentum of a charged particle can be measured from their tracks, according to the relation:

$$p\,[\mathrm{GeV/c}] \;=\; 0.3Br\,[\mathrm{Tm}]. \tag{2.10}$$

The CDC is also used to measure the energy loss (dE/dx) of charged tracks for their particle identification.

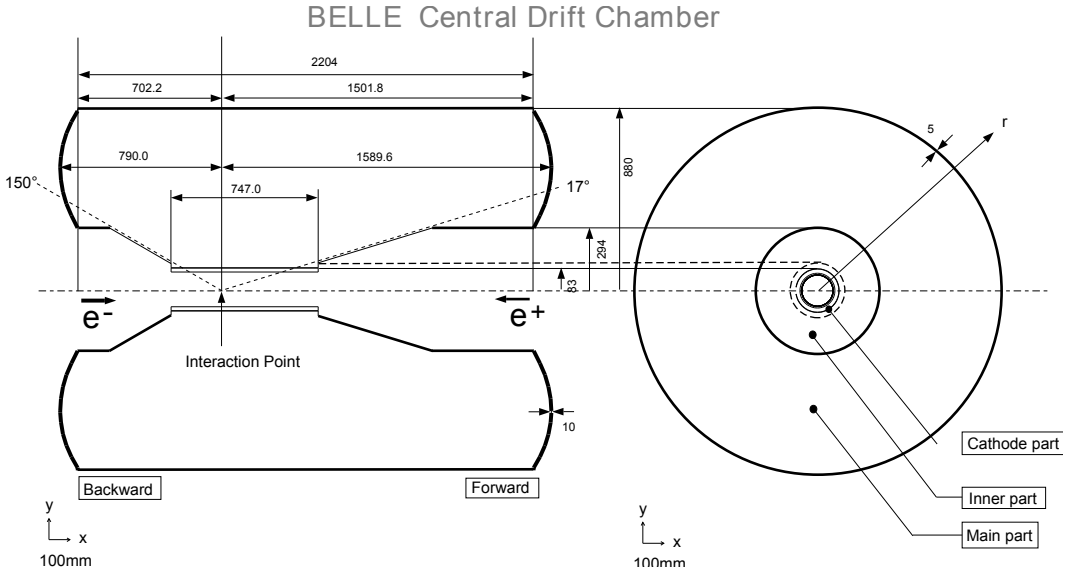

Figure 2.9: Configuration of CDC.

Figure 2.9 shows the CDC geometry. The coverage is $17^\circ \leq \theta \leq 150^\circ$ which corresponds to 92% of the solid-angle. The CDC is a cylindrical chamber with inner radius 83 mm, outer radius 874 mm, and length along the beam pipe 2400 mm. It is filled with gas. Since the majority of the decay products of a B meson have the momentum lower than 1 GeV/c, the minimization of multiple coulomb scattering is important for achieving the precious momentum resolution. For this purpose, a low-Z gas consisting of 50% helium and 50% ethane is chosen. The p_T resolution of the CDC is given by:

$$\sigma_{p_T} \;=\; \left(0.28p_T \oplus \frac{0.35}{\beta}\right)\% \tag{2.11}$$

and this is improved with SVD information as:

$$\sigma_{p_T} \;=\; \left(0.19p_T \oplus \frac{0.30}{\beta}\right)\%. \tag{2.12}$$

The typical p_T resolution is shown in Figure 2.10.

Figure 2.11 shows the measured dE/dx as a function of the particle momentum, together with the expected mean values for different particle species. Populations of pions, kaons, protons and electrons are clearly seen. The dE/dx resolution is measured

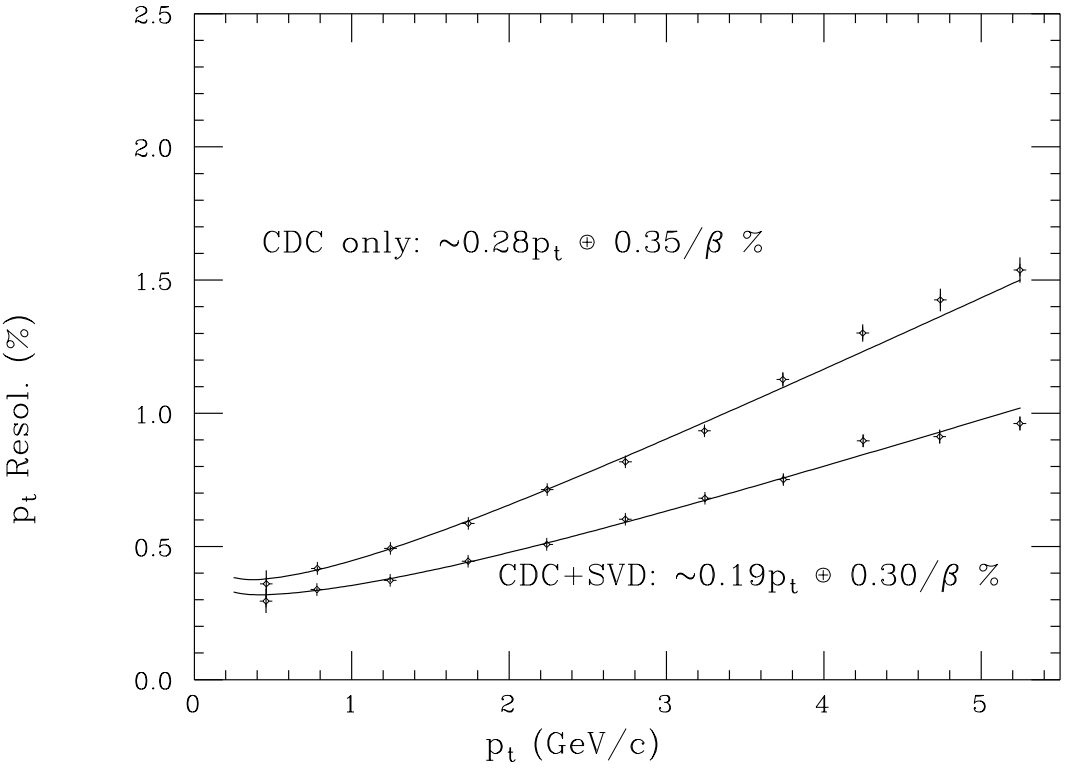

Figure 2.10: The p_T resolution using cosmic ray data.

to be 7.8%. The dE/dx information provides $\geq 3\,\sigma$ K/π separation up to 0.8 GeV/c. The dE/dx also provides more than $3\,\sigma$ e/π separation for the momentum range from 0.3GeV/c to 3 GeV/c.

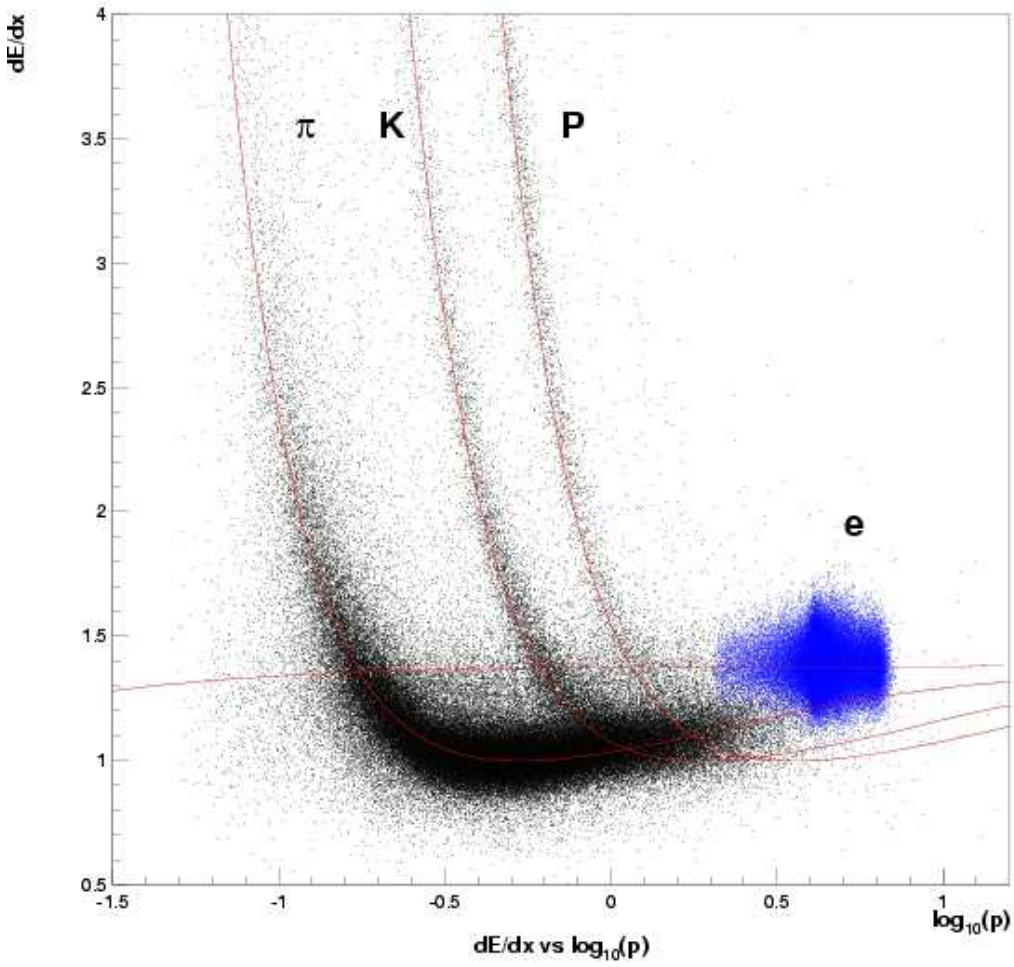

Figure 2.11: dE/dx vs momentum taken from collision data.

2.3.3 Aerogel Cherenkov Counter (ACC)

The Aerogel Cerenkov Counter (ACC) [14] is used for the Belle particle identification system. It brings the capability of identifying high momentum particles (from 1.2 GeV/c to 3.5 GeV/c), which is beyond the reach of dE/dx measurements by CDC and time-of-flight measurements by TOF. Thus, we can distinguish kaons from pions. When a charged particle passes a medium by the speed that exceeds the speed of light in the same medium, Cerenkov radiation is emitted as:

$$n > \frac{1}{\beta} = \sqrt{1 + \left(\frac{m}{p}\right)^2} \tag{2.13}$$

where m and p are the mass and momentum of the particle, and n is the refractive index of the medium. For a fixed n, the threshold energies for the particles to emit Cerenkov photons are proportional to their masses. Thus, we can distinguish kaons from pions to detect emitting Cherenkov radiation, by selecting appropriate medium.

The configuration of ACC is shown in Figure 2.12. The ACC consists two regions, the barrel region and the forward end-cap region. The barrel region consists of 960 counter modules segmented into 60 cells in the φ direction. The forward end-cap region is 228 modules arranged in 5 concentric layers. All the counters are arranged in a semi-tower geometry, pointing to the interaction point, covering a total polar angle range from 17° to 127°. A counter module consists of silica aerogel encased in an aluminum box. One or two photomultiplier tubes are attached to the sides of each box to detect Cherenkov radiation pulses. In order to obtain good K/π separation for the whole kinematic range, the refractive indices of silica aerogel are selected to be between 1.01 and 1.03, depending on their polar angle. For the barrel modules, $n = 1.010$, 1.013, 1.015, 1.020 and 1.028 are used. Silica aerogel with $n = 1.030$ is used in the forward end-cap modules, to distinguish lower momentum particles. A typical ACC module is shown in Figure 2.13.

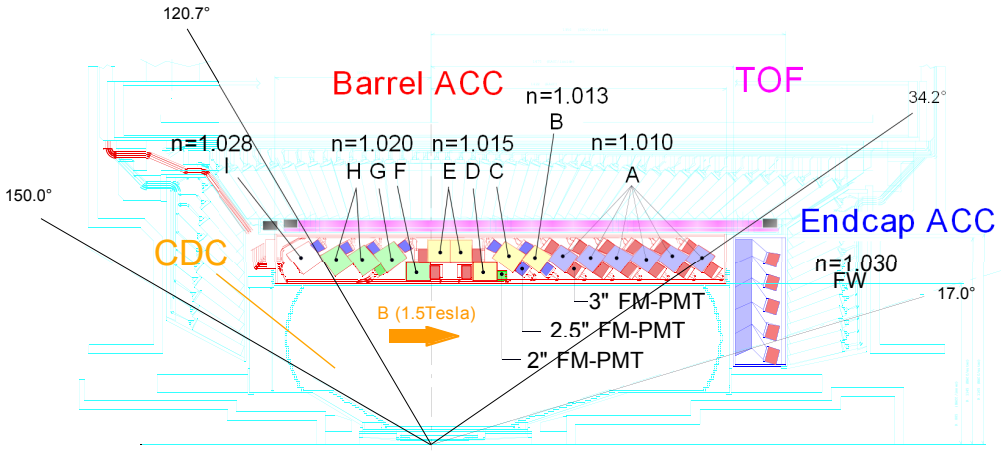

Figure 2.12: The configuration of ACC

Figure 2.14 shows the measured pulse height distributions in the ACC for $\pi^{\pm}$ and $K^{\pm}$ candidates from $D^{*\pm}$ decays, which are selected by TOF and dE/dx measurements. It shows a clear separation between kaons and pions. Good agreement between data and Monte Carlo simulation also can be seen.

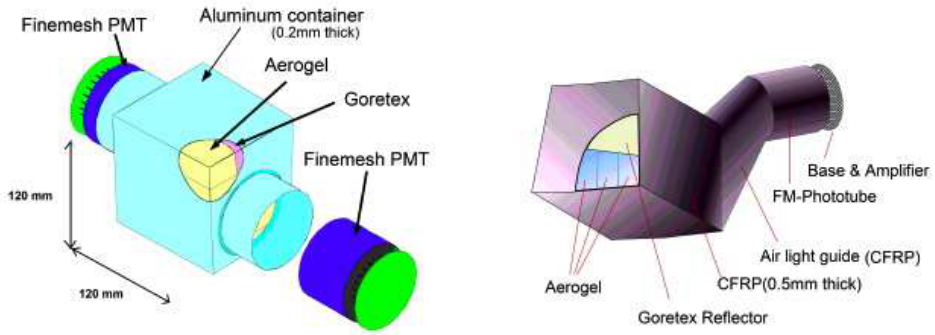

Figure 2.13: ACC barrel module and end-cap module.

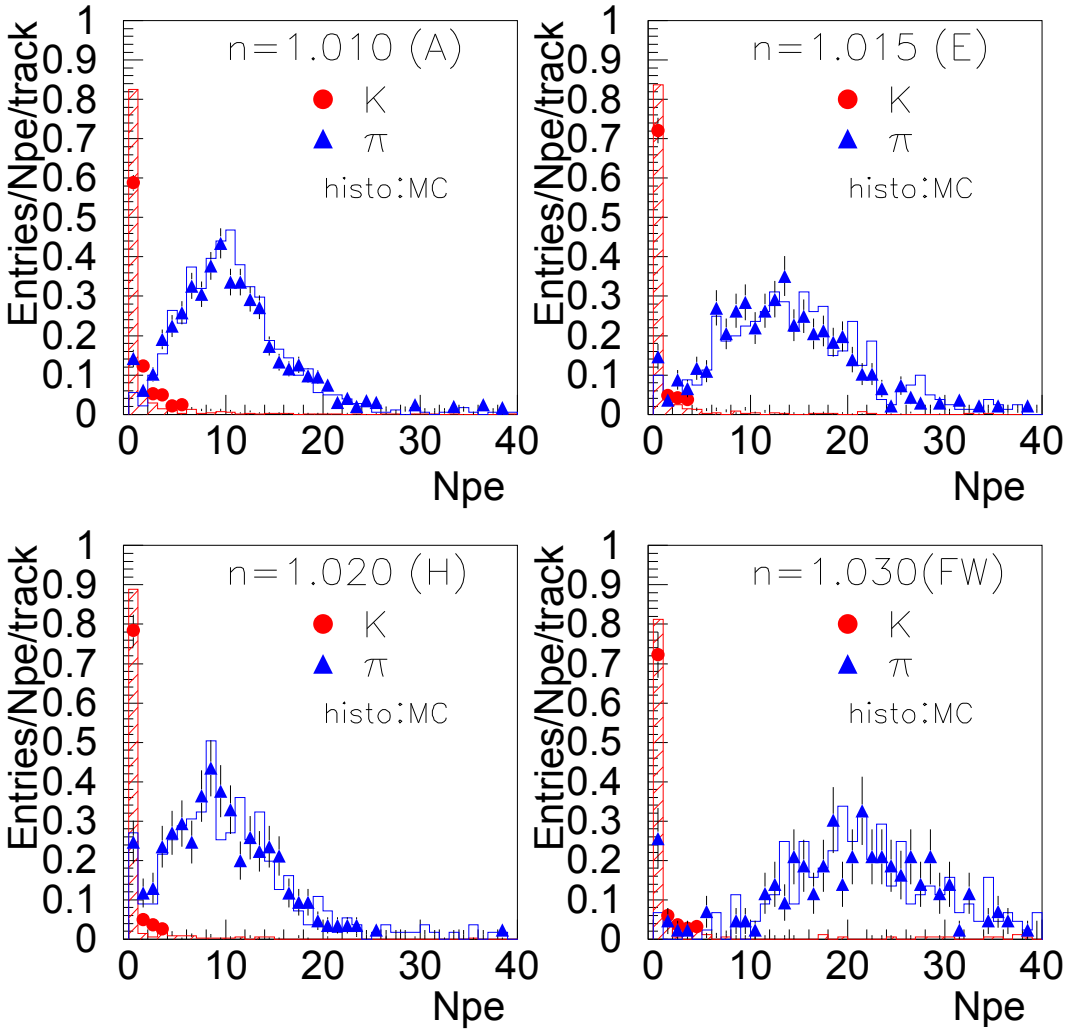

Figure 2.14: Pulse-height spectra in units of photo-electrons for $K^{\pm}$ and $\pi^{\pm}$ in $D^{*\pm}$ decays. Each plot corresponds to the different refractive index.

2.3.4 Time of Flight counter (TOF)

The Time of Flight counter (TOF) [15] provides the particle identification information to distinguish charged kaons from pions in the low momentum region, below 1.2 GeV/c, which encompasses 90% of the particles produced from $\Upsilon(4S)$ decays. The flight time T is expressed as:

$$T = \frac{L}{c\beta} = \frac{L}{c}\sqrt{1+\left(\frac{m}{p}\right)^2} \tag{2.14}$$

where L is a flight length of the particle. The momentum can be provided from CDC, then, TOF can be used for particle identification by calculating the mass of the particle.

TOF system consists of 64 TOF modules. One of TOF modules consists of two plastic scintillation counters (TOF counter) and one thin Trigger Scintillation Counters (TSC). Each TOF (TSC) counter is read out by two (one) fine-mesh photo-multipliers. TOF modules located at a radius of 1.2 m from the IP cover a polar angle range from 33° to 121°. The module geometry is shown in Figure 2.15.

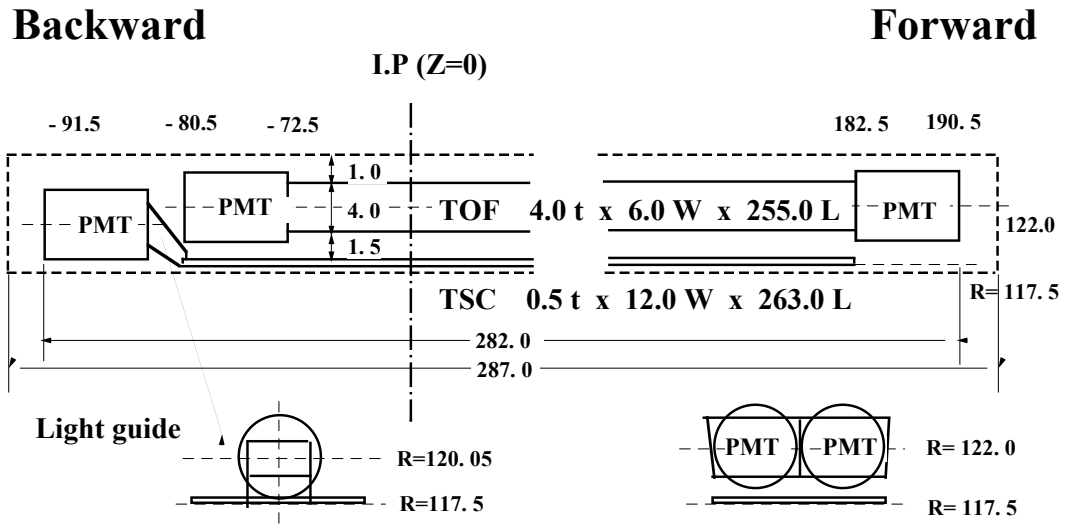

Figure 2.15: TOF module geometry.

Figure 2.16 shows the mass distribution calculated from measured T by TOF. The histogram shows the Monte Carlo results obtained by assuming $\sigma_{\mathrm{TOF}} = 100\,\mathrm{ps}$. The data points are consistent with the simulation prediction. Figure 2.17 shows the K/π separation performance according to the particle momentum.

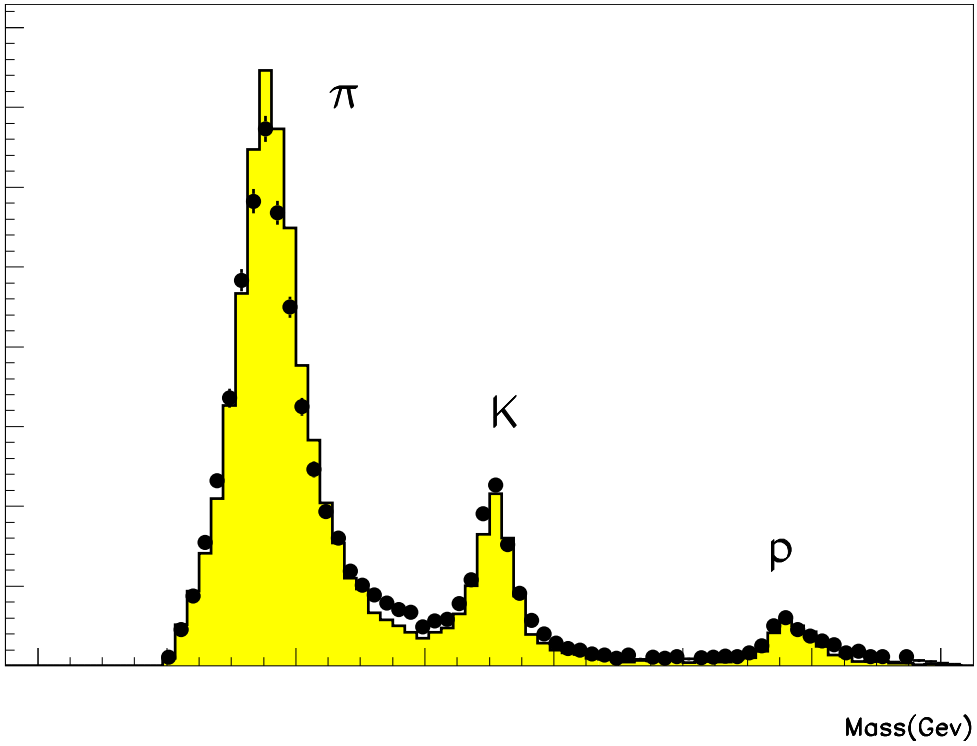

Figure 2.16: Distributions of hadron masses calculated from the measured time-of-flight for particles with momenta less than 1.25 GeV/c.

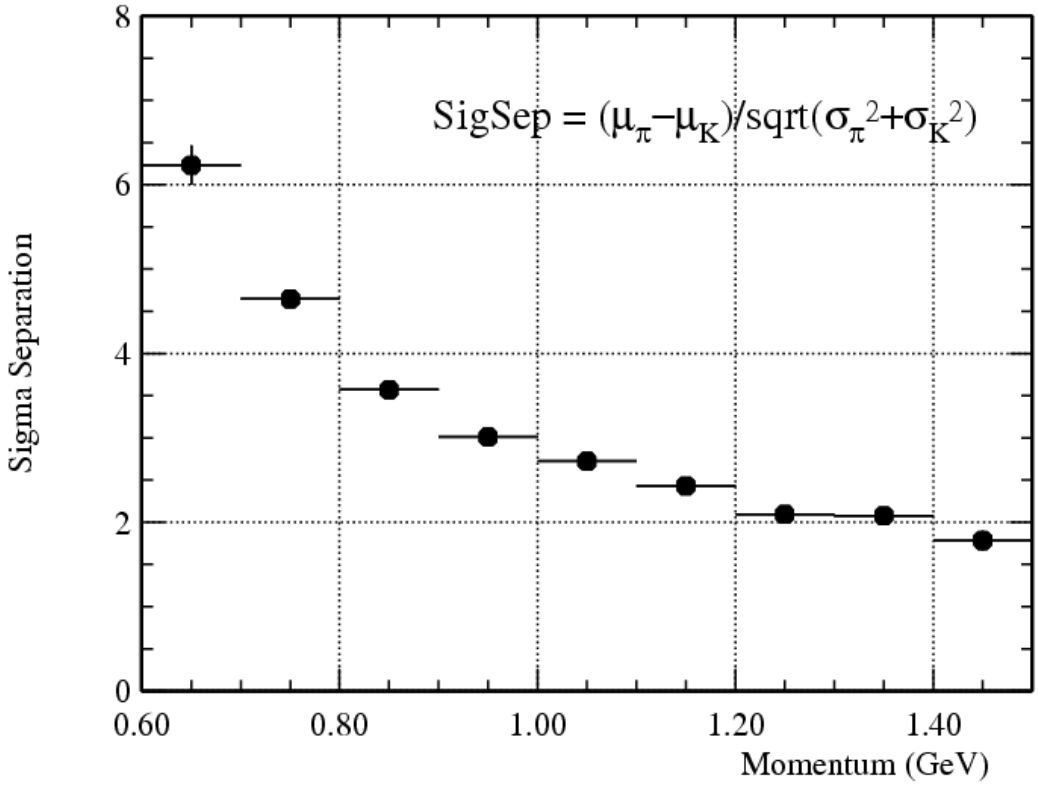

Figure 2.17: K/π separation performance of the TOF.

2.3.5 Electromagnetic Calorimeter (ECL)

The Electromagnetic Calorimeter (ECL) [16] are designed to detect photons and electrons with high efficiency and good resolutions in energy and position. The roles are identification of electrons and reconstruction of π^0 from photons. When an electron or a photon hits the ECL, it loses their energy by bremsstrahlung or electron-positron pair production. These processes repeat over and over again, producing electromagnetic showers. and all of the incident energy is deposited in calorimeter. Other charged particles deposit a small amount of energy by ionization. Therefore, the ratio of the cluster energy measured by the ECL to the momentum of the charged track measured by the CDC, E/p, is close to unity for electrons and lower for other particles. In this way, electron can be identified.

The geometry of the ECL is shown in Figure 2.18. The ECL consists of a barrel section of 3.0 m in length with an inner radius of 1.25 m and annular end-caps at $z = +2.0$ m and $z = -1.0$ m from the interaction point. The ECL consists of 8736 thallium-doped (Tl) CsI crystal counters. They cover the polar angle region of $17^\circ \leq \theta \leq 150^\circ$. A CsI(Tl) crystal is in a tower shape and its length is 30 cm, which corresponds to 16.2 radiation lengths. Each CsI(Tl) crystal points toward the IP. The barrel section has 6624 crystals divided into 46 in θ and 144 in φ. The forward end-cap has 1152 crystals divided into 13 in θ and $48 \sim 144$ in φ depending on θ. The backward has 960 crystals divided into 10 and $64 \sim 144$ in θ and φ, respectively. The geometrical parameters are shown in Table.2.2

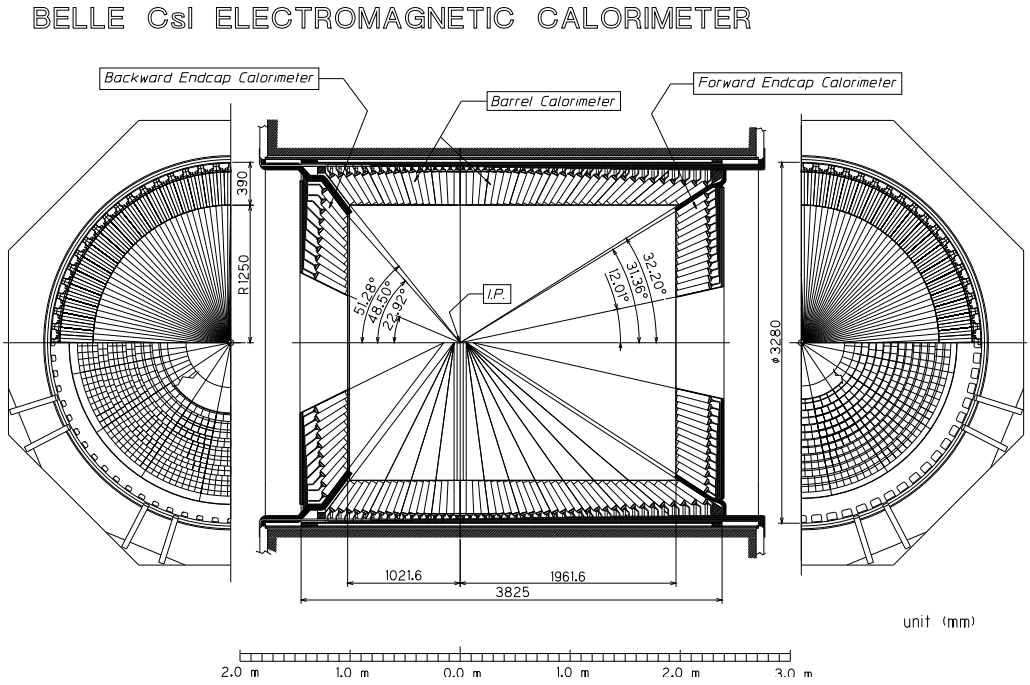

Figure 2.18: ECL geometry.

The energy and position resolution of the ECL are:

$$\frac{\sigma_E}{E} = \left(1.34 \oplus \frac{0.066}{E} \oplus \frac{0.81}{E^{1/4}}\right) \text{ [\%]} \tag{2.15}$$

$$\sigma_{pos} = \left(0.27 + \frac{3.4}{E^{1/2}} + \frac{1.8}{E^{1/4}}\right) \text{ [mm]}. \tag{2.16}$$

Table 2.2: The geometrical parameters of the ECL.

Section	$\theta coverage$	θ segment	φ segment	# of crystals
Forward end-cap	12.4° to 31.4°	13	$48 \sim 144$	1152
Barrel	32.2° *to* 128.7°	46	144	6624
Backward end-cap	130.7° to 155.1°	10	$64 \sim 144$	960

Figure 2.19 shows the energy and position resolution of the ECL. Measurements from the ECL combined those from the CDC, ACC and TOF provide an electron identification efficiency of about 80% and the π fake rate is less than 1% in the momentum range from 500 MeV/c to 2 GeV/c.

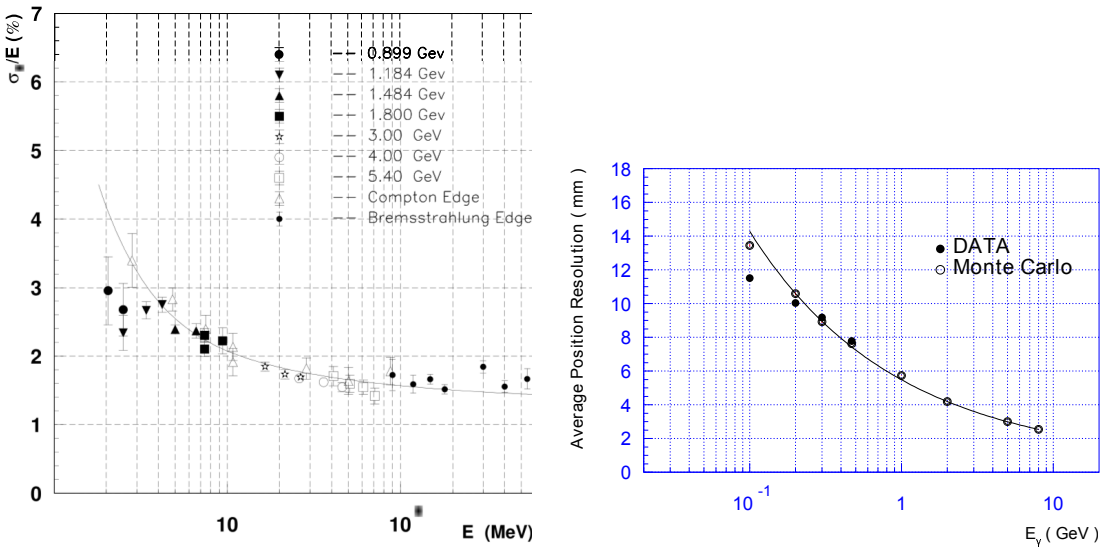

(a) Energy resolution (b) Position resolution

Figure 2.19: Energy and position resolutions of the ECL.

2.3.6 K_L and Muon Detector (KLM)

The purpose of K_L and Muon Detector (KLM) [17] is the identification of K_L and muon with high efficiency. The particle with enough momentum to reach the KLM, greater than 600 MeV/c, is the target to detect. Since they like to penetrate materials, a lot of material is needed to detect them efficiently.

The KLM consists of 4.7 cm thick iron plates and glass resistive plate counters (RPCs) [18]. The KLM is made up of the barrel region and the end-caps in forward and backward. The geometry of the barrel region is shown in Figure 2.20. The barrel region around the IP covers the angular range $45° \leq \theta \leq 125°$ and consists of 15 detector layers and 14 iron layers. Each end-cap consists of 14 detector layers and 14 iron layers and extends the coverage to $20° \leq \theta \leq 155°$. The iron layers have the another role as a return yoke for the magnetic flux provided by the superconducting solenoid. Two RPC modules are consisted RPC super-layer, to provide 2-dimensional θ φ information. Figure 2.21 shows the RPC super-layer.

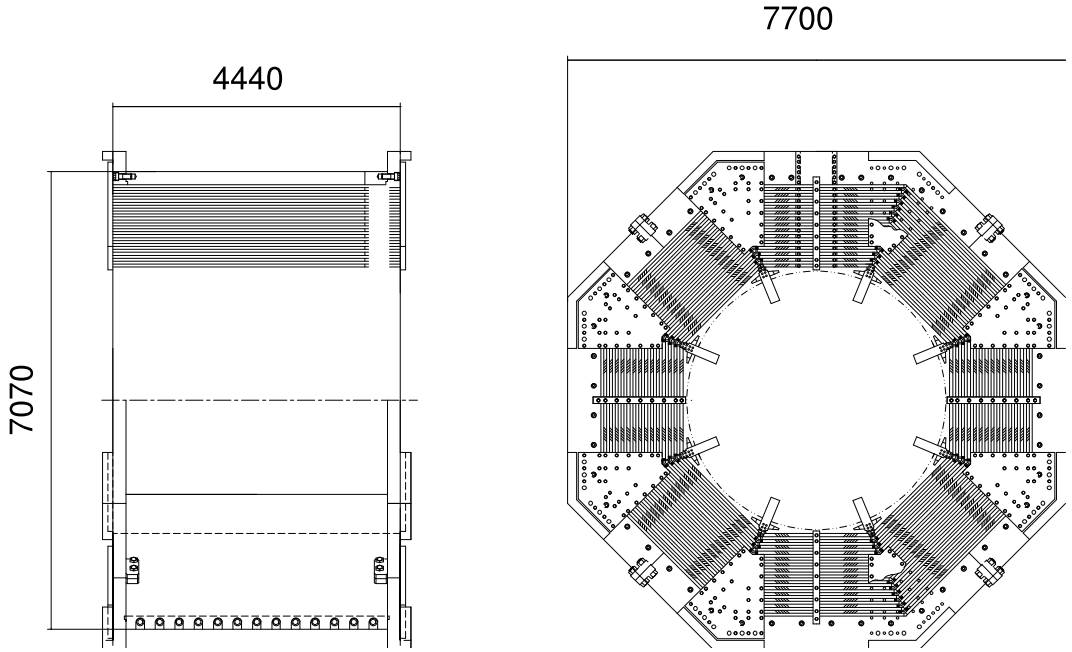

Figure 2.20: The geometry of the KLM.

When hadrons hit the iron plates, a shower of ionizing particles are produced and detected at the RPC layers. K_L may not leave an associated track in the CDC, then, it can be identified. Muons leave the charged tracks, however, they can be distinguished from another charged hadron because of their strong penetration. Hadrons strongly interacts with iron, their trace have wide clusters and are stopped within a few layers of iron. Muons only interact by electromagnetic multiple scattering, so their clusters tend to be thinner and they have far greater penetration depth.

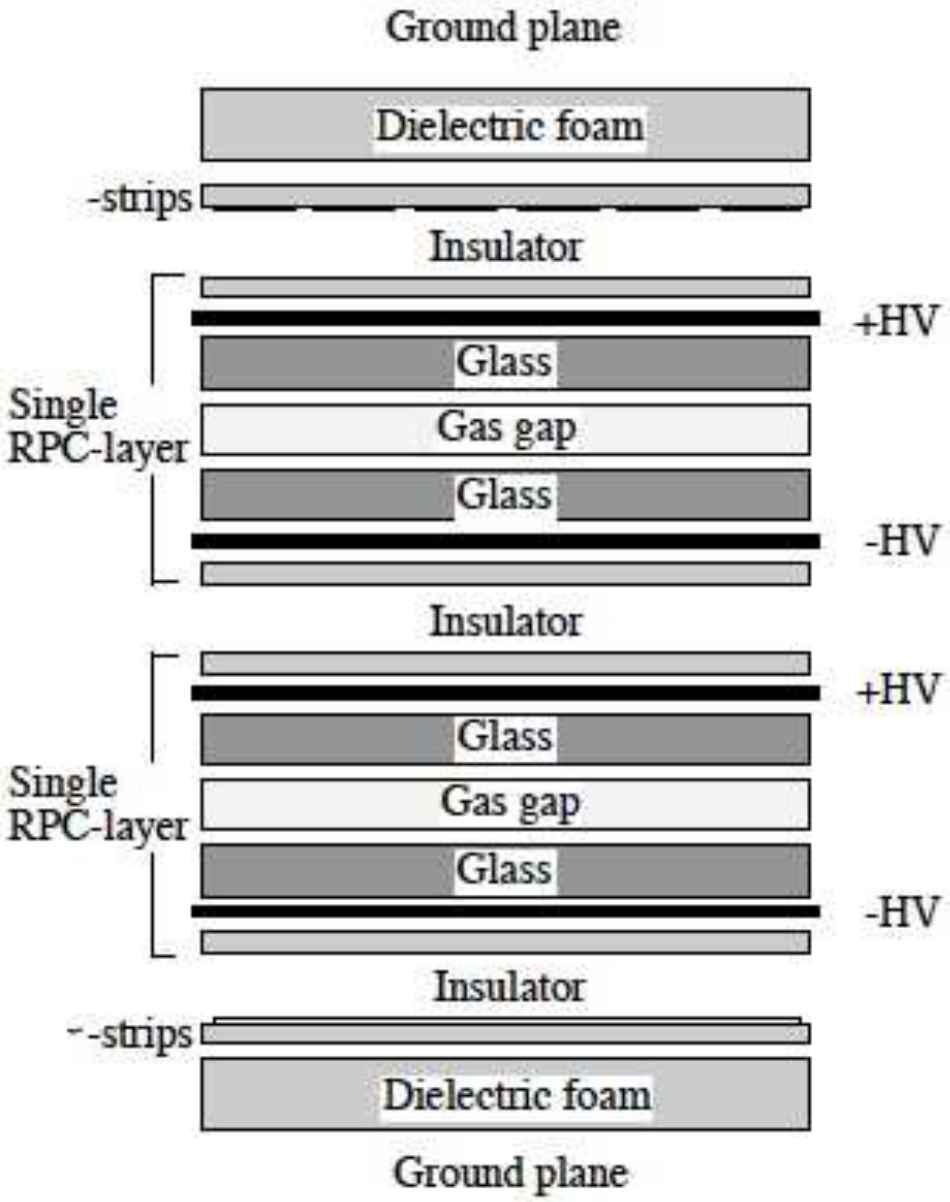

Figure 2.21: Cross section of a RPC super-layer.

2.3.7 Trigger and Data Acquisition

The trigger system (TRG) and the data acquisition system (DAQ) are also important for the Belle experiments. The purpose of the trigger system is to distinguish the interesting events of physics from the large amount of background. Since the background rates are very sensitive to the accelerator conditions at that instant, it is difficult to estimate correctly. Therefore, the trigger system is required to select the interesting events for high efficiency unrelated to the background rates. It is also required to keep the amount of data within the tolerance of the data acquisition system (DAQ). The Belle trigger system consists of the hardware trigger and the software trigger.

The decision to accumulate the events in the data acquisition system (DAQ) is made by the sub-detector trigger systems and the central trigger system called the Global Decision Logic (GDL). Figure 2.22 shows their flow. The trigger system provides a trigger signal at a fixed time, $2.2\,\mu s$, after the beam collision. The trigger efficiency for $B\overline{B}$ events is greater than 99.5%. The sub-detector trigger systems consists with the track triggers and the energy triggers. The CDC and TOF are brought the charged track trigger signals. The ECL provides triggers based on the total energy deposit and the cluster counting of crystal hits. The KLM provided muon trigger. These trigger informations are provide to the GDL.

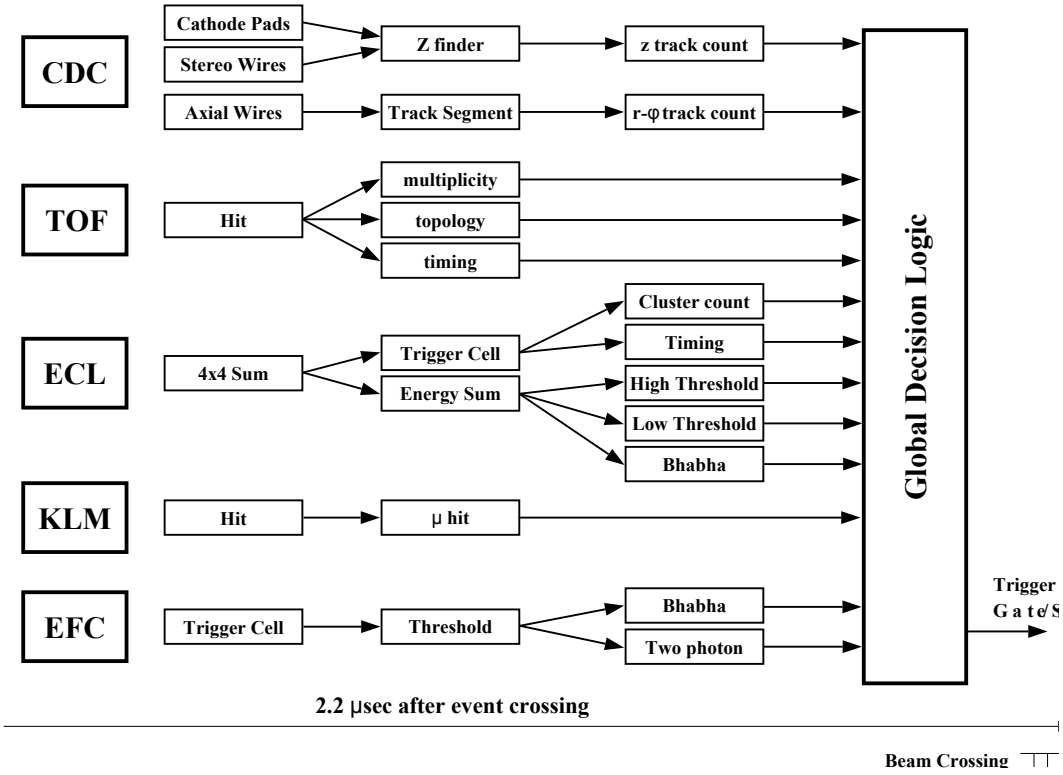

Figure 2.22: Flow of the sub-detector trigger systems and the GDL.

The Belle DAQ system consists of three parts: a front-end readout part, an event building part and a mass storage part. The event builder combines the signals from sub-detectors into a single event and passes it to an online computer farm. In an online computer farm, the events are selected or rejected. The requirements are at least one

track originating from the IP, $dr < 1.0\,\mathrm{cm}$ and $dz < 4.0\,\mathrm{cm}$, with $p_t > 300\,\mathrm{MeV/c}$. Events passing this requirement are then stored in a mass storage system.

Chapter 3

B reconstruction

3.1 Analysis Overview

We explain the extraction procedure of $S^{\pm}$ in Chapter 3 and 4.

We first find the signal decay chain from $B\overline{B}$ pairs accumulated by the Belle detector, which is explained in this chapter. Then $S^{\pm}$ are extracted from time-dependent decay rates of signal, which is explained in chapter 4.

3.2 Data set

3.2.1 Experimental data

Complete data set of 710 fb^{-1} accumulated by the Belle detector is used for this analysis. It contains 770 $\times 10^6$ $B\overline{B}$ pairs. Finite 152 $\times 10^6$ $B\overline{B}$ pairs were collected with SVD1(chapter 2) and the rest were collected with SVD2(chapter 2).

3.2.2 Monte Carlo

For tuning the selection criteria, studying background sources and tuning Δt PDF fitter, we used Monte Carlo (MC) events. They are generated by EVTGEN [19] and detector response is simulated by GSIM. We used two kinds of MC. One is the generic MC where each B decays to all known final states with known branching fractions. It was used for tuning the selection criteria and studying background sources. We generated generic MC events 5 times of the data accumulated by the Belle detector. The other is the signal MC. B-mesons contained in signal MC decay into signal events. The ratio was generated according to the known branching fractions. It was used for tuning Δt PDF fitter. We generated signal MC events 32 times of the real data.

3.3 Event selection

We reconstructed signal events "$B^0(\overline{B^0}) \to D^{*\mp}\pi^{\pm}$" from following decay chains, charge conjugate modes are implied unless explicitly stated:

- $B^0 \to D^{*+}\pi^-$,

- $D^{*+} \to D^0\pi^+, D^+\pi^0$,
- $D^0 \to K^-\pi^+, K^-2\pi^+\pi^-, K^-\pi^+\pi^0, K_s\pi^+\pi^-$,
- $D^+ \to K^-\pi^+\pi^+$.

The reconstruction was according to the following selections.

3.3.1 Charged track selection

To select charged kaons and pions from signal decay, we discarded the tracks which did not have more than one SVD hits in both $r-\phi$ and z directions. Kaons and pions are distinguished by particle identification method defined in Chapter 2. For this analysis, $LR(K,\pi) > 0.3$ and $LR(K,\pi) < 0.7$ are applied for kaons and pions, respectively.

We adopted different selection for slow pions from D^{*+}, with no requirement on SVD hit.

3.3.2 Neutral pion selection

Neutral pions were reconstructed from photon pairs. We selected photon with invariant mass for photon pairs as 0.118 GeV/c^2 to 0.150 GeV/c^2. In addition, to reduce fake π^0 such as wrong combinations of two photons, the photon energy greater than 0.04 GeV was required.

3.3.3 Neutral K selection

We first reconstructed $K_s \to \pi^+\pi^-$ in 30 MeV mass window from PDG value. Then we applied the cut on the following four variables.

- dr : The distance from IP to the tracks in x-y plane.
- $d\phi$: The azimuthal angle between the momentum vector and the decay vertex vector of a K_s candidate.
- z_{dist} : The distance between the two daughter tracks at their interception points.
- fl : The flight length of K_s candidate in x-y plane.

Selection criteria for neutral K are shown in Table 3.1.

Table 3.1: K_s Selection

Momentum (GeV)	dr (cm)	$d\phi$ (rad)	z_{dist} (cm)	fl (cm)
< 0.5	> 0.05	< 0.3	< 0.8	-
0.5 - 1.5	> 0.03	< 0.1	< 1.8	> 0.08
> 1.5	> 0.02	< 0.03	< 2.4	> 0.22

3.3.4 D^0 reconstruction

D^0 was reconstructed from $K^-\pi^+, K^-2\pi^+\pi^-, K^-\pi^+\pi^0, K_s\pi^+\pi^-$ in this analysis. Invariant mass of D^0 reconstructed from $K^-\pi^+\pi^0$ was required to be within $\pm$ 30 MeV/c^2 of PDG value. Others were required to be within $\pm$ 20 MeV/c^2. In addition, a mass constraint fit for D^0 is done with all of it's daughter tracks. A vertex fit was done with the charged daughter tracks. Figure 3.1 (a) $\sim$ (d) shows mass distributions for reconstructed D^0 from real data.

3.3.5 D^+ reconstruction

D^+ was reconstructed from $K^-2\pi^+$ in this analysis. Invariant mass was required to be within $\pm$ 20 MeV/c^2 of PDG value. A mass constraint fit and a vertex fit were done on the same condition with D^0. Figure 3.1 (e) shows D^+ mass distributions.

3.3.6 D^{*+} reconstruction

D^{*+} was reconstructed from $D^0\pi^+$ and $D^+\pi^0$ in this analysis. Invariant mass difference between D^{*+} and D^0 (D^+) is used the selection of D^{*+}. We call the invariant mass difference between D^{*+} and D^0 (D^+) as ΔM. The selection criteria for $D^0\pi^+$ final state and $D^+\pi^0$ final state were 138 MeV/c^2 $< \Delta M <$143 MeV/c^2 and 143 MeV/c^2 $< \Delta M <$148 MeV/c^2, respectively. Figure 3.2 shows ΔM distributions.

3.3.7 B^0 reconstruction

B^0 was reconstructed from $D^{*+}\pi^-$. To select B^0 candidate, we used two variables, ΔE and M_{bc}. ΔE is defined as:

$$\Delta E = E_B^{cms} - E_{beam}^{cms} \tag{3.1}$$

where E_B^{cms} is the energy of reconstructed B and E_{beam}^{cms} is the beam energy. Superscript "cms" means the value in the center-of-mass system of $\Upsilon(4S)$. M_{bc} is the beam constrained mass and defined as:

$$M_{bc} = \sqrt{(E_{beam}^{cms})^2 - (P_B^{cms})^2} \tag{3.2}$$

where P_B^{cms} is the momentum of reconstructed B. Because of higher precision than sum of reconstructed particles, E_{beam}^{cms} are used for calculation.

Signal region was defined as $|\Delta E| < 0.045$ GeV and 5.27 GeV/c^2 $< M_{bc} <$ 5.29 GeV/c^2. To check the background events underneath the signal region, grand side band region was defined as -0.15 GeV $< \Delta E <$ 0.5 GeV and 5.2 GeV/c^2 $< M_{bc} <$ 5.3 GeV/c^2. Best candidate were selected by requiring the minimum χ^2 for M_{bc} and ΔM. Figure 3.3 shows ΔE distributions and figure 3.4 shows M_{bc} distributions.

All selection criteria are shown in Table 3.2. Reconstruction efficiencies for each subdecay are calculated from signal MC and shown in table 3.3. Number of reconstructed B from real data is shown in Table 3.4.

Table 3.2: Selection criteria.

Selection	Requirement
Charged track	
PID for K	$LR(K,\pi) > 0.3$
PID for π	$LR(K,\pi) < 0.7$
SVD hits ($r-\phi$ plane)	≥ 2 except for slow π from D^{*+}
SVD hits (z plane)	≥ 2 except for slow π from D^{*+}
π^0	
invariant mass	0.118 GeV/c^2 $< M_{\pi^0} <$ 0.150 GeV/c^2
photon energy	> 0.04 GeV
K_s	
for momentum of $K_S < 0.5$ GeV	
dr (cm)	> 0.05
$d\phi$ (rad)	< 0.3
z_{dist} (cm)	< 0.8
for 0.5 GeV $<$ momentum of $K_S < 1.5$ GeV	
dr (cm)	> 0.03
$d\phi$ (rad)	< 0.1
z_{dist} (cm)	< 1.8
fl (cm)	> 0.08
for momentum of $K_S > 1.5$ GeV	
dr (cm)	> 0.02
$d\phi$ (rad)	< 0.03
z_{dist} (cm)	< 2.4
fl (cm)	> 0.22
D^0	
D^0 reconstructed from $K^-\pi^+\pi^0$ invariant mass	$\pm 30\,\mathrm{MeV}/c^2$ from PDG value
other D^0 invariant mass	$\pm 20\,\mathrm{MeV}/c^2$ from PDG value
$D^{\pm}$	
invariant mass	$\pm 20\,\mathrm{MeV}/c^2$ from PDG value
$D^{*\pm}$	
$M_{D^{*+}} - M_{D^0}$	138 MeV/c^2 $< \Delta M <$ 143 MeV/c^2
$M_{D^{*+}} - M_{D^+}$	143 MeV/c^2 $< \Delta M <$ 148 MeV/c^2
B^0 grand side band	
ΔE	-0.15 GeV$< \Delta E <$0.5 GeV
M_{bc}	5.2 GeV/c^2 $< M_{bc} <$ 5.3 GeV/c^2
B^0 signal region	
ΔE	-0.045 GeV$< \Delta E <$0.045 GeV
M_{bc}	5.27 GeV/c^2 $< M_{bc} <$ 5.29 GeV/c^2

Table 3.3: Reconstruction efficiency.

Decay mode	Efficiency(SVD1)	Efficiency(SVD2)
$D^0 \to K^-\pi^+$	27.8%	38.3%
$D^0 \to K^-2\pi^+\pi^-$	13.1%	22.5%
$D^0 \to K^-\pi^+\pi^0$	11.5%	15.4%
$D^0 \to K_s\pi^+\pi^-$	9.3%	15.5%
$D^+ \to K^+2\pi^-$	8.9%	13.8%

Table 3.4: Number of reconstructed B from real data.

Decay mode	# of B
$D^0 \to K^-\pi^+$	18581±136
$D^0 \to K^-2\pi^+\pi^-$	22465±150
$D^0 \to K^-\pi^+\pi^0$	24018±155
$D^0 \to K_s\pi^+\pi^-$	5344±73
$D^+ \to K^+2\pi^-$	7657±88

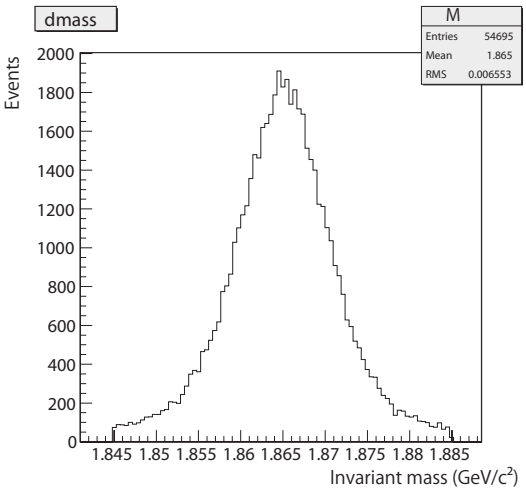

(a) $D^0 \to K^-\pi^+$

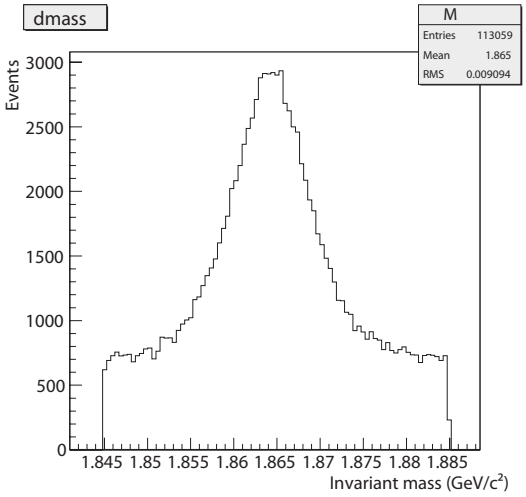

(b) $D^0 \to K^-\pi^+\pi^+\pi^-$

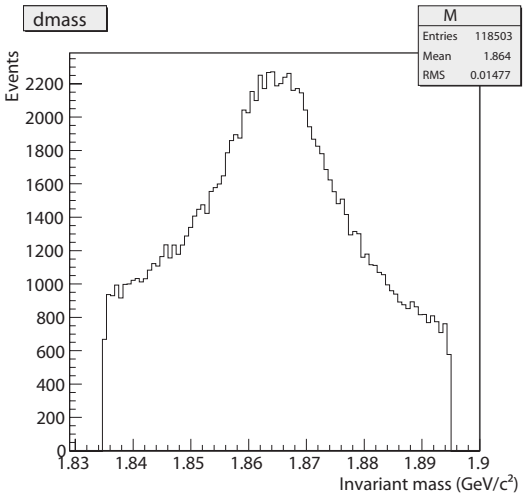

(c) $D^0 \to K^-\pi^+\pi^0$

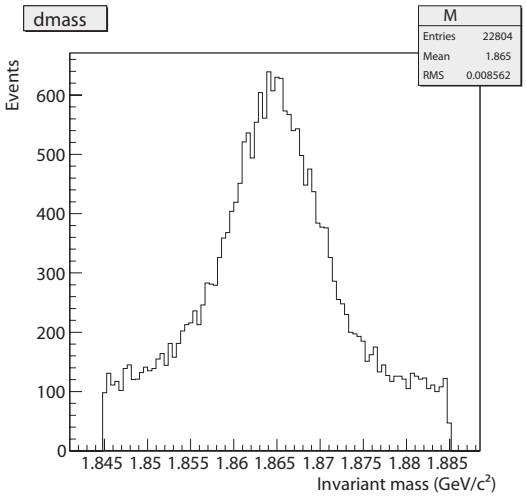

(d) $D^0 \to K_s\pi^+\pi^-$

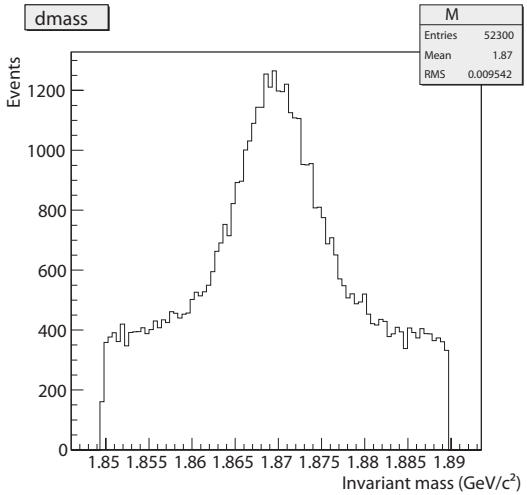

(e) $D^+ \to K^-\pi^+\pi^+$

Figure 3.1: $D^0(D^+)$ mass distribution

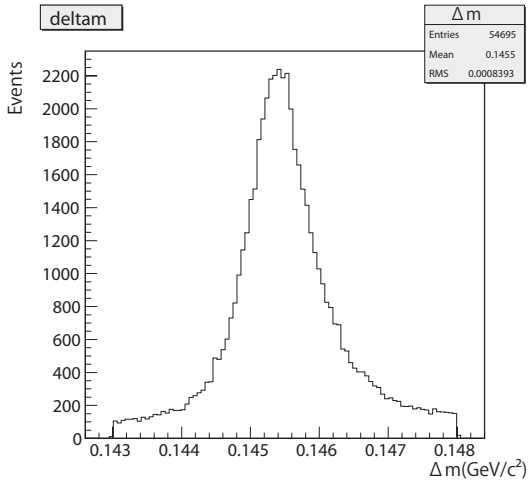

(a) $D^0 \to K\pi$

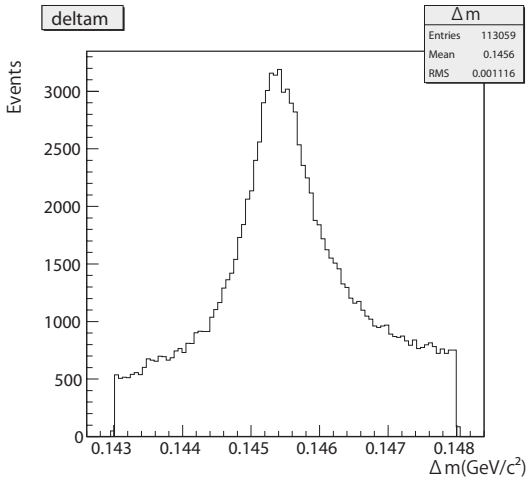

(b) $D^0 \to K\pi\pi\pi$

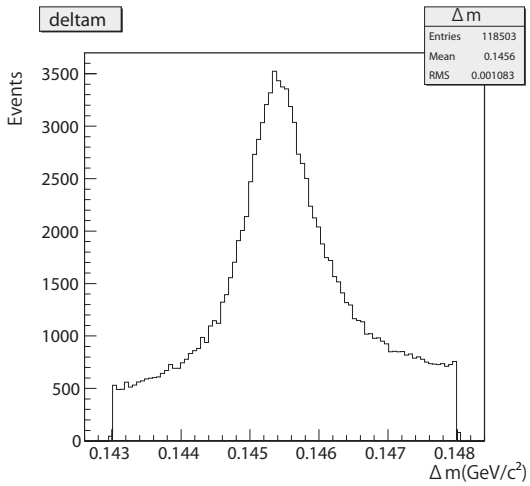

(c) $D^0 \to K\pi\pi^0$

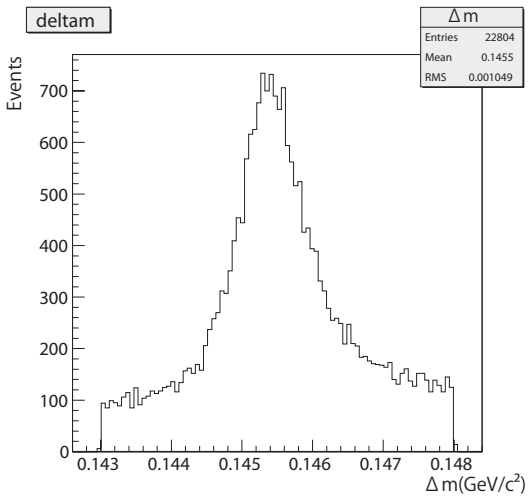

(d) $D^0 \to K_s\pi\pi$

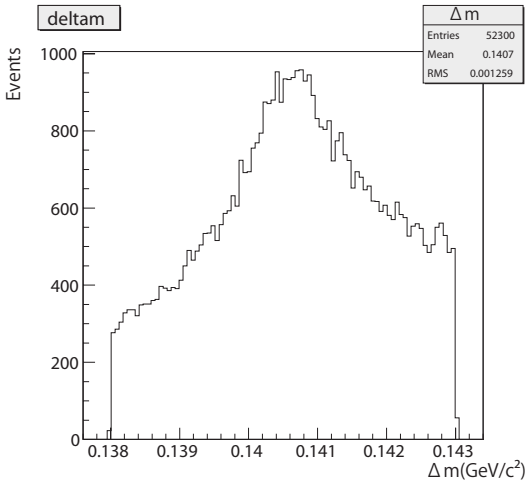

(e) $D^{\pm} \to K\pi\pi$

Figure 3.2: ΔM distribution

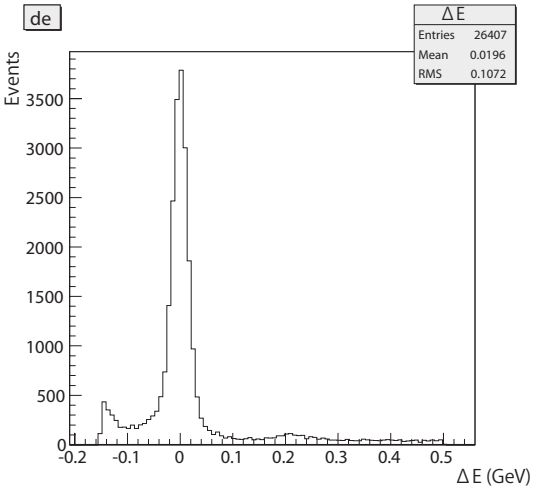

(a) $D^0 \to K\pi$

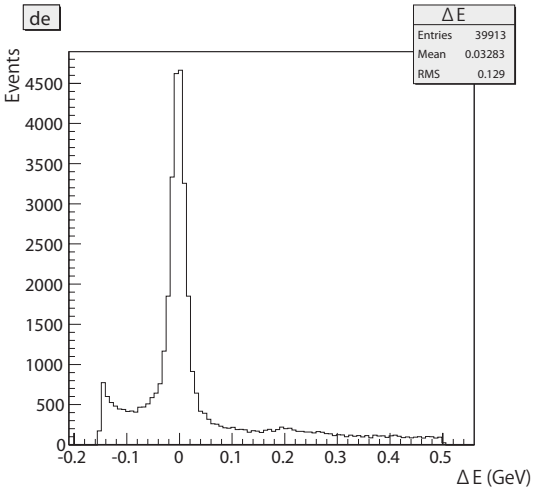

(b) $D^0 \to K\pi\pi\pi$

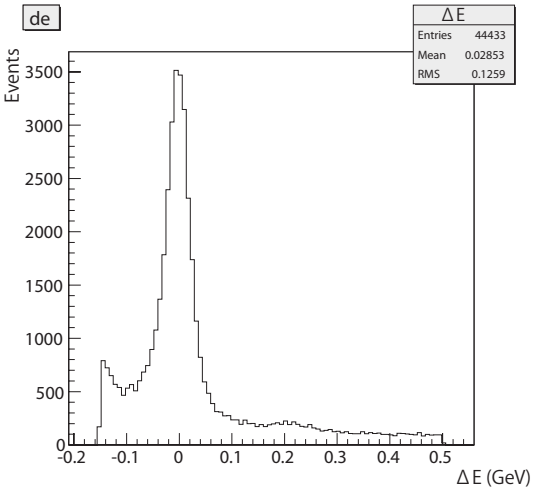

(c) $D^0 \to K\pi\pi^0$

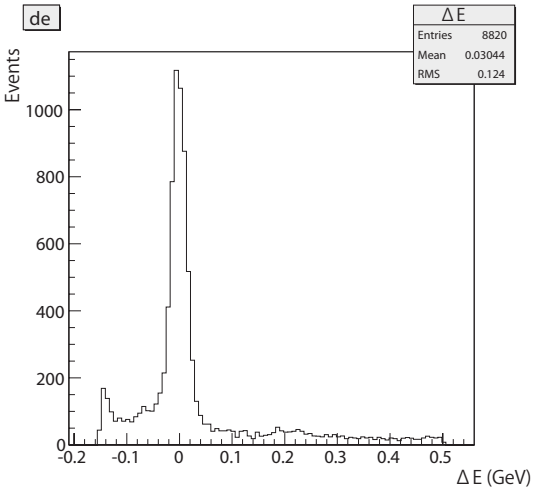

(d) $D^0 \to K_s\pi\pi$

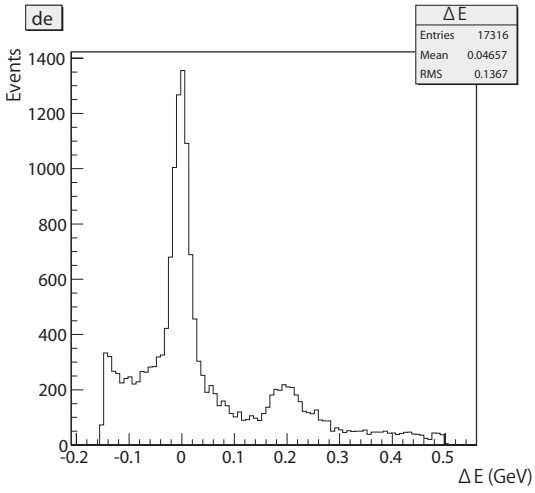

(e) $D^{\pm} \to K\pi\pi$

Figure 3.3: ΔE distribution in M_{bc} signal region.

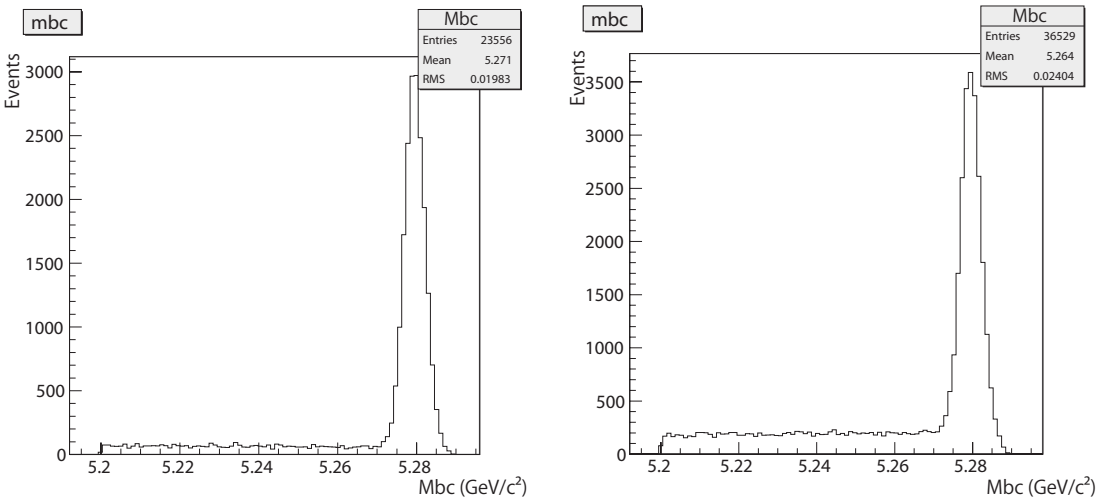

(a) $D^0 \to K\pi$

(b) $D^0 \to K\pi\pi\pi$

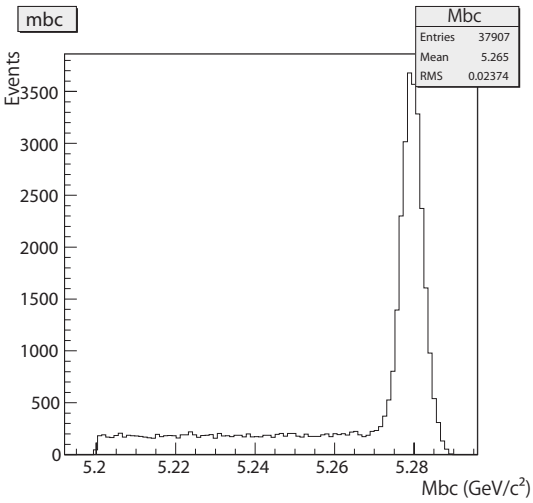

(c) $D^0 \to K\pi\pi^0$

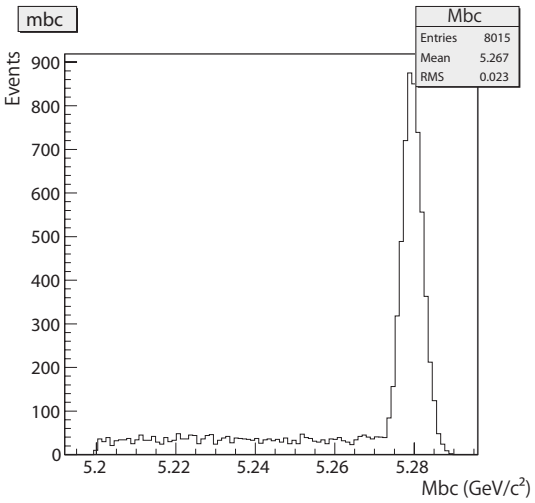

(d) $D^0 \to K_s\pi\pi$

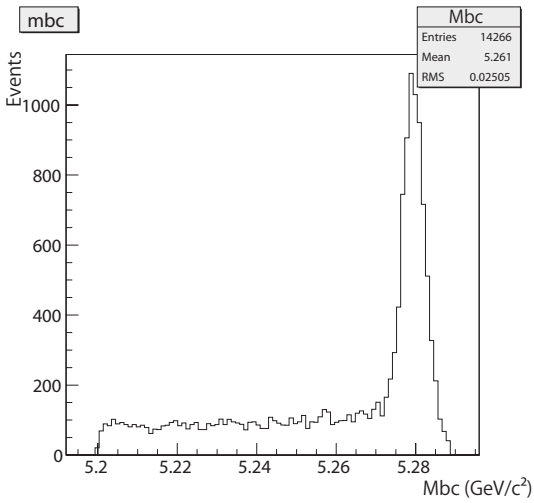

(e) $D^{\pm} \to K\pi\pi$

Figure 3.4: M_{bc} distribution in ΔE signal region.

3.4 Flavor tag

Since B^0 and $\overline{B}^0$ can decay into $D^{*\pm}\pi^{\mp}$, the flavor of a reconstructed B cannot be determined by itself. The flavor was identified by the other side B. We call it tag-side B. $\Upsilon(4S)$ is $S = 1$ and $B^0(\overline{B}^0)$ is $S = 0$, then, the orbital angular momentum of B-pair equals 1. Commutation relation is an anti-symmetrical state. B-pair, therefore, cannot be identical particles. We identified the flavor of the tag-side B at the decay time of it.

We determined the flavor of the tag-side B based on the informations of the final state particles. There are several flavor specific decay modes of the b quark that can be used to determine its flavor.

- high-momentum leptons from $B^0 \to Xl^+\nu$ decays (Figure.3.5)
- intermediate-momentum leptons from $\overline{b} \to \overline{c} \to \overline{s}l^-\overline{\nu}$ decays (Figure.3.5)
- kaons, since the majority of them originate from $B^0 \to K^+X$ decays through the cascade transition $\overline{b} \to \overline{c} \to \overline{s}$
- $\overline{\Lambda}$ baryons from the cascade decay $\overline{b} \to \overline{c} \to \overline{s}$
- high momentum pions coming from $B^0 \to D^{(*)}\pi^+X$ decays (Figure.3.6)
- slow pions from $B^0 \to D^{*-}X, D^{*-} \to \overline{D}^0\pi^-$ decays (Figure.3.6)

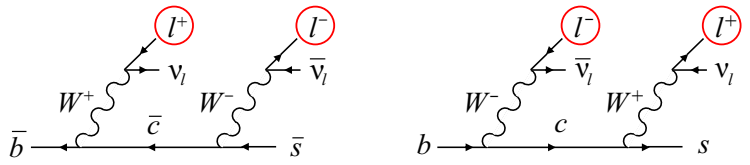

Figure 3.5: Flavor tagging with leptons

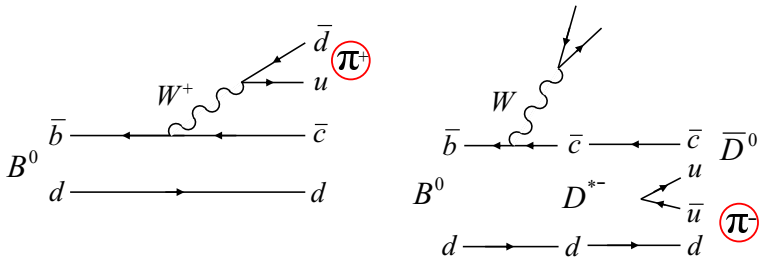

(a) high momentum pion (b) slow pion

Figure 3.6: Flavor tagging with pions

We use two parameters, q and r, for the flavor tagging and its accuracy. The parameter q represents the flavor of the tag-side B. When $q = +1(-1)$, tag-side B is a $B^0(\overline{B}^0)$. The parameter r is an expected flavor dilution factor that ranges from zero for no flavor information to unity for unambiguous flavor assignment. We prepared the look-up table which outputs q and r according to the final states. The signed probability, $q{\cdot}r$, is given by:

$$q{\cdot}r = \frac{N(B^0) - N(\overline{B}^0)}{N(B^0) + N(\overline{B}^0)} \tag{3.3}$$

where $N(B^0)$ and $N(\overline{B}^0)$ are the numbers of B^0 and $\overline{B}^0$ in each bin of the look-up table prepared from a large statistics MC event sample.

We express the wrong tag fraction as w. The relation of r and w is:

$$r = 1 - 2w. \tag{3.4}$$

If w is calculated from r, it has potential for bias because of the difference between real-data and MC simulation. To prevent it we segmentalize it according to r (Table.3.5) and $w_{r-bin}(r-bin = 0{\sim}6)$ in each segment are measured. Semi-leptonic decay $B^0{\to}D^{(*)-}l^+\nu$ and hadronic decay $B^0{\to}D^{*-}\pi^+$, $D^{*-}\rho^+$ was used for measurement of w_{r-bin}. Events in the segment of r-bin $= 0$ hardly has the information for flavor identification, therefore w_0 is fixed at 0.5. We measured the wrong tag fraction by signal MC. They consisted with the wrong tag fraction that measured by MC of above decay mode. The comparisons of the wrong tag fraction are shown in Table.3.6 and 3.7, where w is the average of the wrong tag fraction of B^0 and $\overline{B^0}$, and Δw is the difference between the wrong tag fraction of B^0 and $\overline{B^0}$. The wrong tag fraction from real data of above decay mode were used for time dependent analysis of $B^0{\to}D^{*\pm}\pi^{\mp}$.

Table 3.5: The flavor tagging category based on r

r-bin	r				
0	0.1	$\geq$	r	$\geq$	0
1	0.25	$\geq$	r	$>$	0.1
2	0.5	$\geq$	r	$>$	0.25
3	0.625	$\geq$	r	$>$	0.5
4	0.75	$\geq$	r	$>$	0.625
5	0.875	$\geq$	r	$>$	0.75
6	1.	$\geq$	r	$>$	0.875

Table 3.6: The comparison of the wrong tag fraction

r-bin	w of signal MC	reference w of MC	reference w of Data
0		0.5	0.5
1	0.418679	0.420827	0.418852 +0.007236 -0.006002
2	0.306554	0.300296	0.329879 +0.007129 -0.006431
3	0.217922	0.219317	0.233898 +0.007418 -0.007693
4	0.157096	0.154636	0.170608 +0.006886 -0.006416
5	0.0912084	0.0916131	0.099791 +0.0067610 -0.0088078
6	0.0241709	0.0228891	0.0228501 +0.0043367 -0.0045876

Table 3.7: The comparison of Δw

r-bin	Δw of signal MC	reference Δw of MC	reference Δw of Data
0		0.0	0.0
1	0.0002607	0.0583019	0.0569661 +0.0089233 -0.0091655
2	0.00121148	0.00573998	0.0126192 +0.0091807 -0.0091474
3	0.00616917	-0.0392635	-0.0147724 +0.0103518 -0.0099888
4	-0.0042785	0.00474508	-0.000550289 +0.009020215 -0.008879500
5	0.0024612	-0.0118737	0.00887704 +0.00930821 -0.00929498
6	-0.00225408	-0.00585326	0.00465683 +0.00569346 -0.00578797

Chapter 4

Time dependent analysis of $B^0 \to D^*\pi$ decays

4.1 Difference between $B^0\overline{B^0}$ pair decay time Δt

The difference between $B^0\overline{B^0}$ pair decay time is given by:

$$\Delta t \equiv t_{sig} - t_{tag} \tag{4.1}$$

where t_{sig} and t_{tag} are the decay time of signal-side $B(B_{sig})$ and tag-side $B(B_{tag})$ respectively. B_{sig} represents B which has decayed into $D^{*+}\pi^-$. B_{tag} represents B which has been generated from the same $\Upsilon(4S)$ as B_{sig}. Δt has a time scale of pico-second, therefore it cannot be measured directly. We calculate Δt from the decay vertices of B_{sig} and B_{tag}. Since B_{sig} and B_{tag} are almost stationary with respect to $\Upsilon(4S)$ rest frame, typical velocity of them is about third part of the speed of light and $\Upsilon(4S)$ is strongly boosted to the direction of beam-pipe ($z-$axis), Δt is expressed as:

$$\Delta t \simeq \frac{\Delta z}{\beta\gamma c} \tag{4.2}$$

where Δz is the difference between the decay vertices of B_{sig} and B_{tag} in z-axis. $\beta\gamma$ is Lorentz boost factor. Since the collision energy at Belle is constant, the velocity of B is also constant and $\beta\gamma \sim 0.425$.

The decay vertex of B_{sig} is reconstructed from the charged tracks and $D^0(D^\pm)$ momentum. Because of the finite lifetime of D^0 and $D^\pm$, it is necessary to roll back the daughter particles of $D^0(D^\pm)$ according to $D^0(D^\pm)$ momentum. The decay vertex of B_{tag} is reconstructed from the charged tracks that are not associated with B_{sig}.

4.2 Fit procedure

Unbinned maximum likelihood fits to the four time-dependent decay rates ($B^0 \to D^{*+}\pi^-$, $B^0 \to D^{*-}\pi^+$, $\overline{B}^0 \to D^{*-}\pi^+$, $\overline{B}^0 \to D^{*+}\pi^-$) are performed to extract $S^\pm$. In this fit, $-2lnL \equiv -2\Sigma_i lnL_i$ are minimized, where L_i is a likelihood for i-th event given by:

$$L_i = (1 - f_{ol})[f_{sig}P_{sig} \otimes R_{sig} + (1 - f_{sig})P_{bkg} \otimes R_{bkg}] + f_{ol}P_{ol} \tag{4.3}$$

$$P_{bkg}\otimes R_{bkg} \equiv f_{B^0}P_{B^0}\otimes R_{B^0} + f_{B^\pm}P_{B^\pm}\otimes R_{B^\pm} + (1 - f_{B^0} - f_{B^\pm})P_{con}\otimes R_{con} \quad (4.4)$$

where $f_{sig,\,B^0,\,B^\pm}$ are the signal/background fractions, $P_{sig,\,B^0,\,B^\pm,\,con,\,ol}$ are the probability density functions and $R_{sig,\,B^0,\,B^\pm,\,con}$ are the Δt resolution functions.

The $f_{sig,\,B^0,\,B^\pm}$ are determined on an event-by-event using ΔE value, r and $D^{0(+)}$ decay mode. We provided the fixed ΔE PDF with respect to each $D^{0(+)}$ decay mode and each r-bin as a reference. We reconstructed generic MC and divided the events into signal, continuum background and the background from $B^{0(\pm)}$ decay. We fixed the shape of ΔE PDF for $B^{0(\pm)}$ background by fitting each samples. We include the self cross feed in signal, where the self cross feed represents the event which has been mistaken K^+ for π^+ and π^+ for K^+ at the same event. The ratio in signal and the shape of ΔE PDF for self cross feed were fixed by generic MC. Then we reconstructed real data and fitted ΔE PDF to the events with respect to $D^{0(+)}$ decay mode and r-bin. We use floating double-Gaussian and a line for signal and continuum background, respectively. ΔE PDFs for each $D^{0(+)}$ decay mode and each r-bin are determined. The $f_{sig,\,B^0,\,B^\pm}$ for an event are extracted from the ΔE PDF according to ΔE value. Figure 4.1 shows ΔE plot of real data, combined in all r-bin of SVD2.

The P_{sig}, P_{B^0}, $P_{B^\pm}$ and P_{con} are signal PDF, neutral B background PDF, charged B background PDF and continuum background PDF, respectively. P_{ol} explains an outlier component which has a very long tail described as a single gaussian with a width of about 40 ps. We explain them in next section.

The Δt resolution functions, denoted by R_{sig}, R_B^0, $R_B^\pm$ and R_{con}, are determined on event-by-event basis, using the estimated uncertainties on the z vertex positions [20][21]. $R(\Delta t)$ is represented by convolution of four resolution components as follows:

$$R(\Delta t) = R_{rec}(\Delta t)\otimes R_{asc}(\Delta t)\otimes R_{np}(\Delta t)\otimes R_k(\Delta t). \quad (4.5)$$

- $R_{rec}(\Delta t)$: B_{sig} decay vertex resolution
- $R_{asc}(\Delta t)$: B_{tag} decay vertex resolution
- $R_{np}(\Delta t)$: a non-primary track effect in the B_{tag} vertex reconstruction
- $R_k(\Delta t)$: an effect from the kinematic approximation that B mesons are produced at rest frame in the $\Upsilon(4S)$

The detector resolution functions $R_{rec}(\Delta t)$ and $R_{asc}(\Delta t)$ are a sum of two gaussians:

$$R_{rec}(\Delta t) = (1 - f_{rec}^{tail})G(\Delta t; s_{rec}^{main}\cdot\sigma_{rec}) + f_{rec}^{tail}G(\Delta t; s_{rec}^{tail}\cdot\sigma_{rec}) \quad (4.6)$$

$$R_{asc}(\Delta t) = (1 - f_{asc}^{tail})G(\Delta t; s_{asc}^{main}\cdot\sigma_{asc}) + f_{asc}^{tail}G(\Delta t; s_{asc}^{tail}\cdot\sigma_{asc}) \quad (4.7)$$

where f is a minor part fraction of two gaussians, s is the scale factor and σ is the error of the vertex reconstruction. $G(t;\sigma)$ is a gaussian defined by:

$$G(t;\sigma) \equiv \frac{1}{\sqrt{2\pi}\sigma}\exp\left(-\frac{x^2}{2\sigma^2}\right). \quad (4.8)$$

$R_{np}(\Delta t)$ is a sum of Dirac's delta function and exponential function:

$$R_{np}(\Delta t) = f_\delta\cdot\delta(\Delta t) + (1 - f_\delta)\cdot[f_p\cdot E_p(\Delta t;\tau_p) + (1 - f_p)\cdot E_n(\Delta t;\tau_n)] \quad (4.9)$$

where

$$E_p(t;\tau) \equiv \frac{1}{\tau}\exp(-\frac{t}{\tau}) \quad \text{for } t \geq 0, \text{ otherwise } 0 \tag{4.10}$$

$$E_n(t;\tau) \equiv \frac{1}{\tau}\exp(+\frac{t}{\tau}) \quad \text{for } t \leq 0, \text{ otherwise } 0. \tag{4.11}$$

If B_{tag} decays into lepton, f_δ is set to 1.

$R_k(\Delta t)$ is changed to be dependent on cosine of an angle between B momentum in center of mass system and z-axis ($\cos\theta_B$). If $\cos\theta_B = 0$, $R_k(\Delta t)$ is delta function. Otherwise $R_k(\Delta t)$ is exponential function.

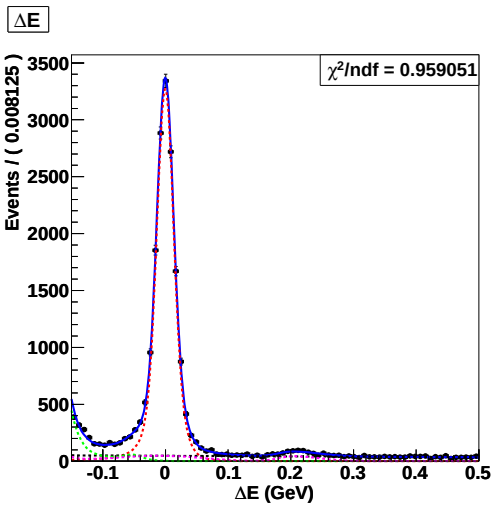

(a) $D^0 \to K\pi$

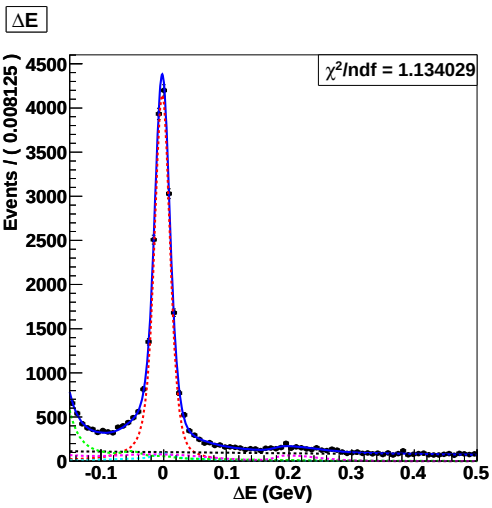

(b) $D^0 \to K\pi\pi\pi$

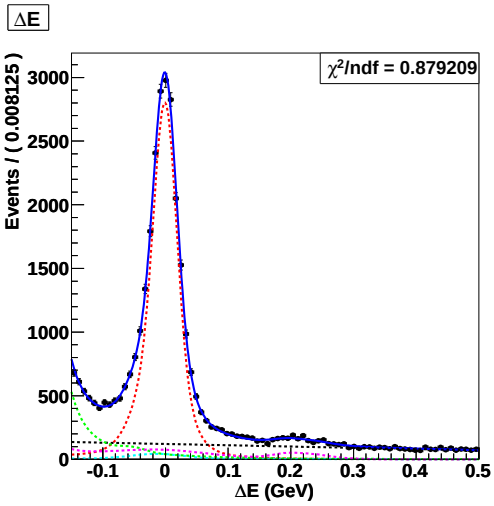

(c) $D^0 \to K\pi\pi^0$

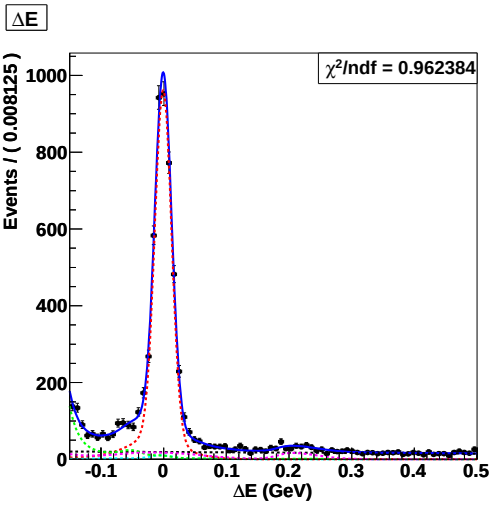

(d) $D^0 \to K_s\pi\pi$

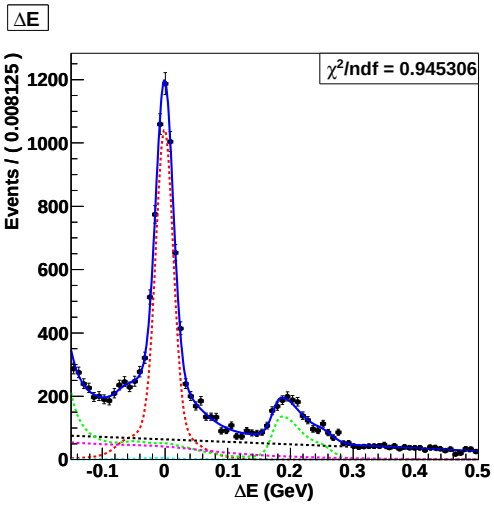

(e) $D^{\pm} \to K\pi\pi$

Figure 4.1: ΔE PDF. Red line is signal PDF, black dashed line is continuum BG PDF, green line is B^0 BG PDF and magenta line is $B^{\pm}$ BG PDF.

4.3 Probability Density Function for Δt

4.3.1 signal PDF

Signal events include an event with correct identification and an event with wrong identification with respect to flavor, B^0 or $\overline{B}^0$. Using the wrong tag fraction w, signal PDF are described as:

$$P_{sig}(q=-1; B_{sig}\to D^{*\mp}\pi^{\pm}) = (1-w_{\overline{B^0}})P(B^0\to D^{*\mp}\pi^{\pm}) + w_{B^0}P(\overline{B^0}\to D^{*\mp}\pi^{\pm}) \quad (4.12)$$

$$P_{sig}(q=+1; B_{sig}\to D^{*\pm}\pi^{\mp}) = (1-w_{B^0})P(\overline{B^0}\to D^{*\pm}\pi^{\mp}) + w_{\overline{B^0}}P(B^0\to D^{*\pm}\pi^{\mp}) \quad (4.13)$$

$$P(B^0\to D^{*\mp}\pi^{\pm}) = \frac{e^{-\frac{|\Delta t|}{\tau_{B^0}}}}{8\tau_{B^0}}[1\pm Ccos(\Delta m\Delta t) - S^{\mp}sin(\Delta m\Delta t)] \quad (4.14)$$

$$P(\overline{B^0}\to D^{*\pm}\pi^{\mp}) = \frac{e^{-\frac{|\Delta t|}{\tau_{B^0}}}}{8\tau_{B^0}}[1\pm Ccos(\Delta m\Delta t) + S^{\pm}sin(\Delta m\Delta t)]. \quad (4.15)$$

tag side interference

Tag-side decay can have a CPV, like signal-side decay, called tag side interference (TSI) [22]. Measured $S^{\pm}$ include this effect. $S^{\pm}$ are described as:

$$S^+_{fav} = S^+ + S^-_{tag} \quad (4.16)$$

$$S^+_{sup} = S^+ - S^+_{tag} \quad (4.17)$$

$$S^-_{fav} = S^- + S^+_{tag} \quad (4.18)$$

$$S^-_{sup} = S^- - S^-_{tag} \quad (4.19)$$

where subscript fav and sup represent favored mode and suppressed mode, respectively, and $S^{\pm}_{tag}$ is time-dependent CP violating parameters for TSI described as:

$$S^{\pm}_{tag} = -2\frac{R'}{1-2R'^2}sin(2\phi_1+\phi_3\pm\delta'). \quad (4.20)$$

To measure the $S^{\pm}_{tag}$, $B^0\to D^{*-}l^+\nu$ sample without lepton tag events were used [23][24]. $B^0\to D^{*-}l^+\nu$ were reconstructed and it has no CPV from reconstructed B. CPV which is measured by $B^0\to D^{*-}l^+\nu$ therefore come from tag-side B. Observed TSI is as follows:

$$S^+_{tag} = -0.0096\pm0.0073 \quad (4.21)$$

$$S^-_{tag} = +0.0067\pm0.0073. \quad (4.22)$$

4.3.2 background Δt shape

Background Δt shapes were determined for continuum, neutral B and charged B background with respect to SVD1 and SVD2. For the background PDF, we used:

$$P_{con} = f_\delta \cdot \delta(\Delta t - \mu_\delta) + (1 - f_\delta) exp(-\frac{|\Delta t - \mu_{exp}|}{\tau_{con}}) \quad (4.23)$$

$$P_{B^0BG} = \frac{exp(-\frac{|\Delta t|}{\tau_{B^0BG}})}{8\tau_{B^0BG}} \{1 - q_{tag} q_{rec} (1 - 2w_{rbin}) cos(\Delta m \Delta t)\} \quad (4.24)$$

$$P_{B^\pm BG} = \frac{exp(-\frac{|\Delta t|}{\tau_{B^\pm}})}{8\tau_{B^\pm}} \{1 - q_{tag} q_{rec} (1 - 2w_{rbin})\} \quad (4.25)$$

where $q_{tag,rec}$ are the parameters of B flavor, $q_{tag,rec} = +1(-1)$ represent B is a $B^0(\overline{B}^0)$.

Resolution function for continuum background is described as:

$$R_{con} = (1 - f_{con}^{tail}) G(\Delta t; s_{con}^{main} \cdot \sigma_{vtx}) + f_{con}^{tail} G(\Delta t; s_{con}^{tail} \cdot \sigma_{vtx}). \quad (4.26)$$

The background shape parameters for B^0 and $B^\pm$ were determined by the fitting to generic MC. For continuum BG, real data in $\Delta E - M_{bc}$ sideband region were used for fitting. The fit results are shown in Table 4.1 and Figure 4.2.

Table 4.1: Background shape parameters

Parameters	SVD1	SVD2
continuum		
f_{δ}^{mlt}	0.557 ± 0.0778	0.436 ± 0.021
f_{tail}^{mlt}	0.040 ± 0.012	0.033 ± 0.004
s_{main}^{mlt}	1.246 ± 0.048	1.293 ± 0.020
s_{tail}^{mlt}	5.83 ± 0.794	6.257 ± 0.314
f_{δ}^{sgl}	0.455 ± 0.139	0.281 ± 0.040
f_{tail}^{sgl}	0.213 ± 0.063	0.060 ± 0.006
s_{main}^{sgl}	0.857 ± 0.087	1.143 ± 0.031
s_{tail}^{sgl}	3.302 ± 0.398	12.586 ± 1.683
$\mu_{exp}^{con}(ps)$	0.127 ± 0.062	-0.005 ± 0.013
$\mu_{\delta}^{con}(ps)$	-0.097 ± 0.036	0.008 ± 0.010
$\tau_{con}(ps)$	0.764 ± 0.091	0.809 ± 0.024
neutral B		
τ_{B^0BG}	1.410 ± 0.038	1.480 ± 0.014
Δm_{B^0BG}	0.541 ± 0.040	0.545 ± 0.012
$w_1^{B^0BG}$	0.453 ± 0.036	0.450 ± 0.014
$w_2^{B^0BG}$	0.327 ± 0.034	0.320 ± 0.012
$w_3^{B^0BG}$	0.207 ± 0.039	0.228 ± 0.014
$w_4^{B^0BG}$	0.245 ± 0.044	0.209 ± 0.016
$w_5^{B^0BG}$	0.133 ± 0.038	0.111 ± 0.014
$w_6^{B^0BG}$	0.067 ± 0.031	0.067 ± 0.010
charged B		
$\tau_{B^{\pm}BG}$	1.648 ± 0.049	1.589 ± 0.015
$w_1^{B^{\pm}BG}$	0.496 ± 0.029	0.472 ± 0.010
$w_2^{B^{\pm}BG}$	0.352 ± 0.031	0.352 ± 0.009
$w_3^{B^{\pm}BG}$	0.222 ± 0.032	0.260 ± 0.011
$w_4^{B^{\pm}BG}$	0.133 ± 0.025	0.156 ± 0.010
$w_5^{B^{\pm}BG}$	0.074 ± 0.021	0.126 ± 0.010
$w_6^{B^{\pm}BG}$	0.016 ± 0.011	0.043 ± 0.006

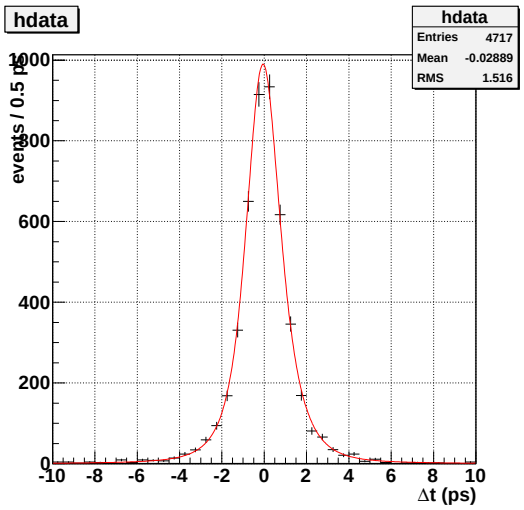

(a) continuum BG of SVD1 real data in side band region(0.3 GeV< ΔE <0.5 GeV, 5.2 GeV/c^2 < M_{bc} <5.26 GeV/c^2)

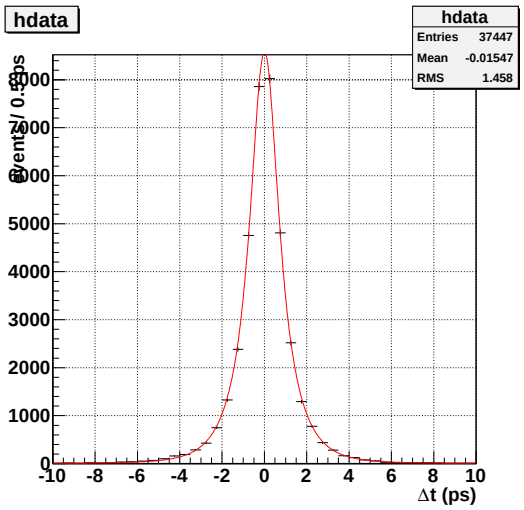

(b) continuum BG of SVD2 real data in side band region(0.3 GeV< ΔE <0.5 GeV, 5.2 GeV/c^2 < M_{bc} <5.26 GeV/c^2)

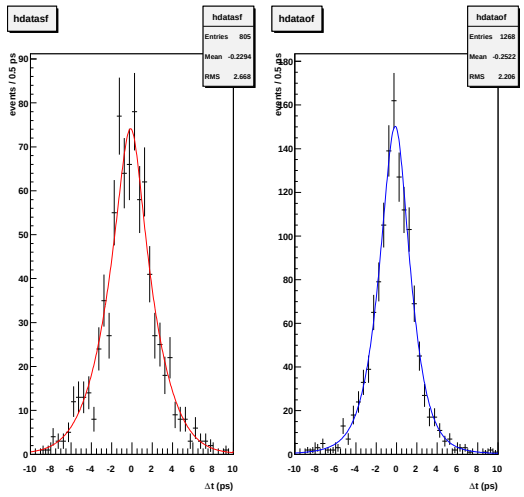

(c) neutral B BG of SVD1 generic MC in signal region

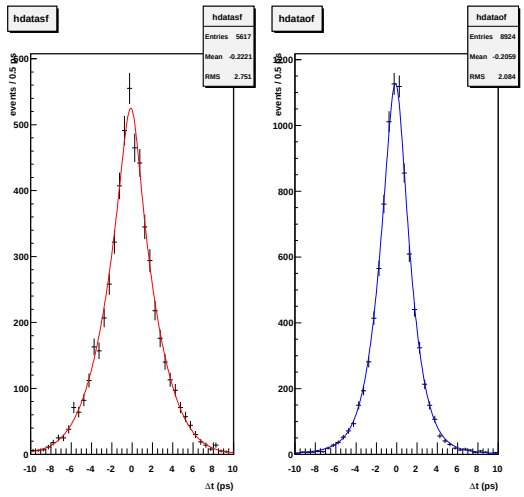

(d) neutral B BG of SVD2 generic MC in signal region

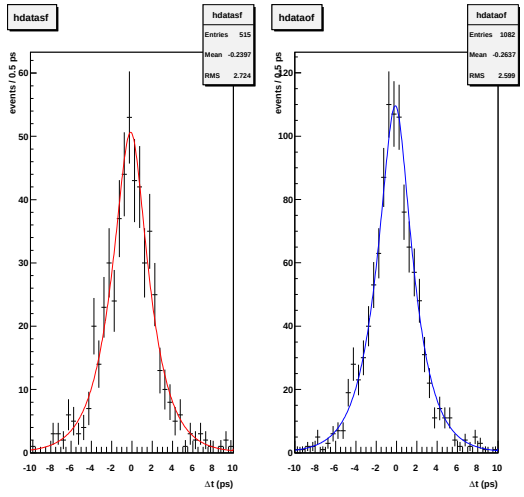

(e) charged B BG of SVD1 generic MC in signal region

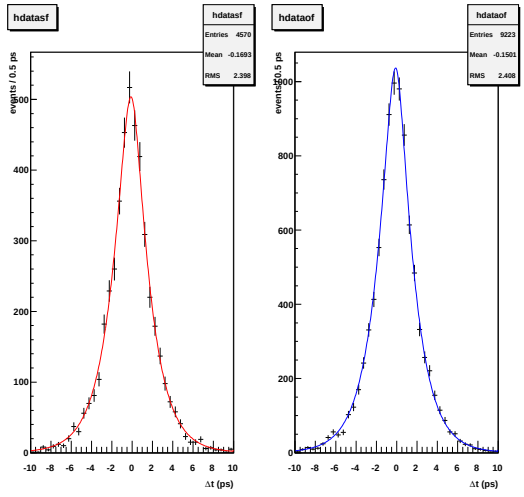

(f) charged B BG of SVD2 generic MC in signal region

Figure 4.2: P_{bkg} plot

4.4 Extraction of B^0 lifetime and $B^0\overline{B^0}$ mixing parameter

To check the validity of the fitting procedure, the lifetime of B^0 and the mixing parameter of $B^0\overline{B^0}$ were extracted and compared with world average. To extract them, we have combined B^0 events and $\overline{B^0}$ events. As a result of the combination, signal PDF for favored mode and suppressed mode becomes:

$$\begin{aligned} P_{sig,\,fav} &= \frac{e^{-\frac{|\Delta t|}{\tau_{B^0}}}}{4\tau_{B^0}}[1+(1-w_{B^0}-w_{\overline{B^0}})(Ccos(\Delta m\Delta t)+(S^+-S^-)sin(\Delta m\Delta t)] \\ &\simeq \frac{e^{-\frac{|\Delta t|}{\tau_{B^0}}}}{4\tau_{B^0}}[1+C(1-w_{B^0}-w_{\overline{B^0}})cos(\Delta m\Delta t)] \end{aligned} \tag{4.27}$$

$$\begin{aligned} P_{sig,\,sup} &= \frac{e^{-\frac{|\Delta t|}{\tau_{B^0}}}}{4\tau_{B^0}}[1+(1-w_{B^0}-w_{\overline{B^0}})(Ccos(\Delta m\Delta t)-(S^+-S^-)sin(\Delta m\Delta t)] \\ &\simeq \frac{e^{-\frac{|\Delta t|}{\tau_{B^0}}}}{4\tau_{B^0}}[1-C(1-w_{B^0}-w_{\overline{B^0}})cos(\Delta m\Delta t)] \end{aligned} \tag{4.28}$$

where σ, in any case small, is ignored, then CP violating term are canceled.

We fitted τ_B^0 and Δm using the data which were accumulated by Belle. Above resolution function and background PDF were used. We obtained the values that are consistent with world averages as shown in Table 4.2. Figure 4.3 and Figure 4.4 show the Δt plot and the mixing asymmetry, respectively.

Table 4.2: life time and mixing parameter fit results of the data which were accumulated by Belle

Parameters	fit results	world average
$\tau_{B^0}(ps)$	1.532±0.007	1.519±0.007
$\Delta m(ps^{-1})$	0.505 ± 0.005	0.507 ± 0.004

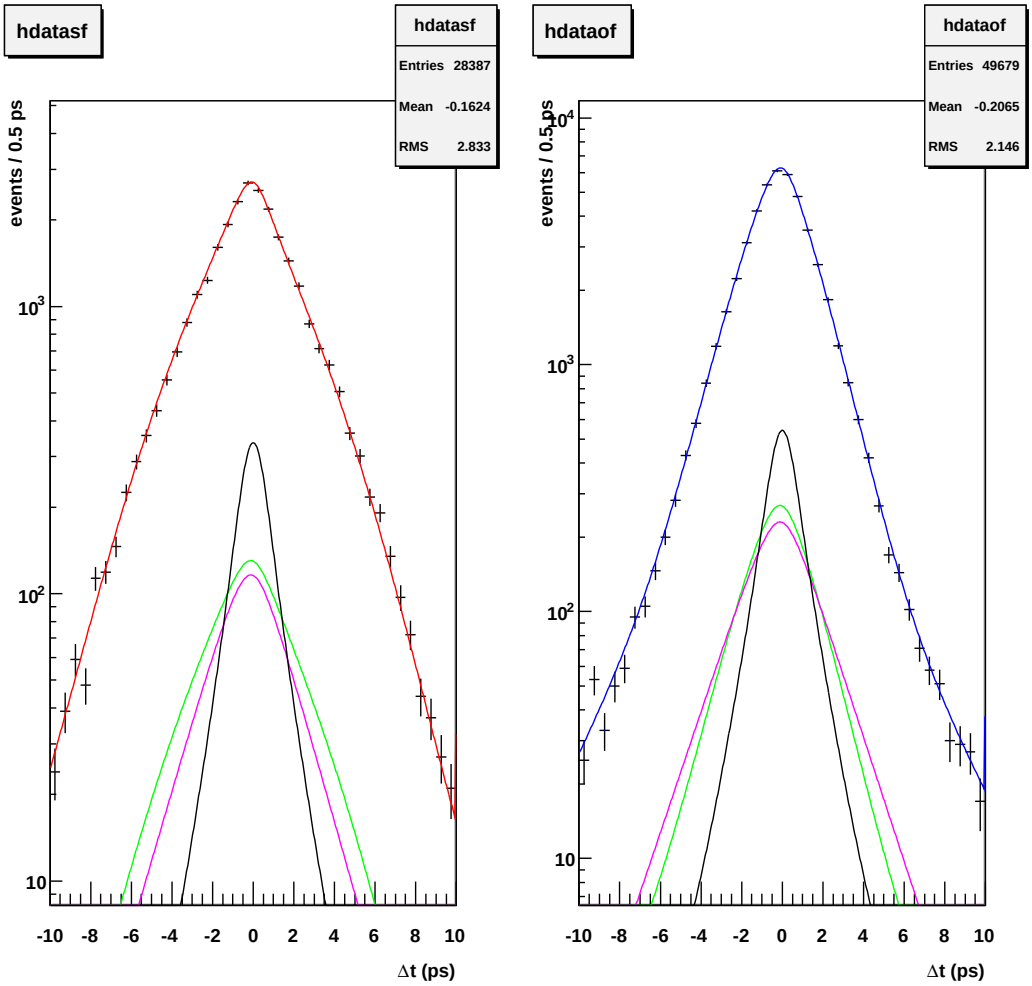

Figure 4.3: Δt distribution of the data which were accumulated by Belle. Left plot is suppressed mode and right plot is favored mode. Black line is continuum BG, green line is B^0 BG and magenta line is $B^{\pm}$ BG.

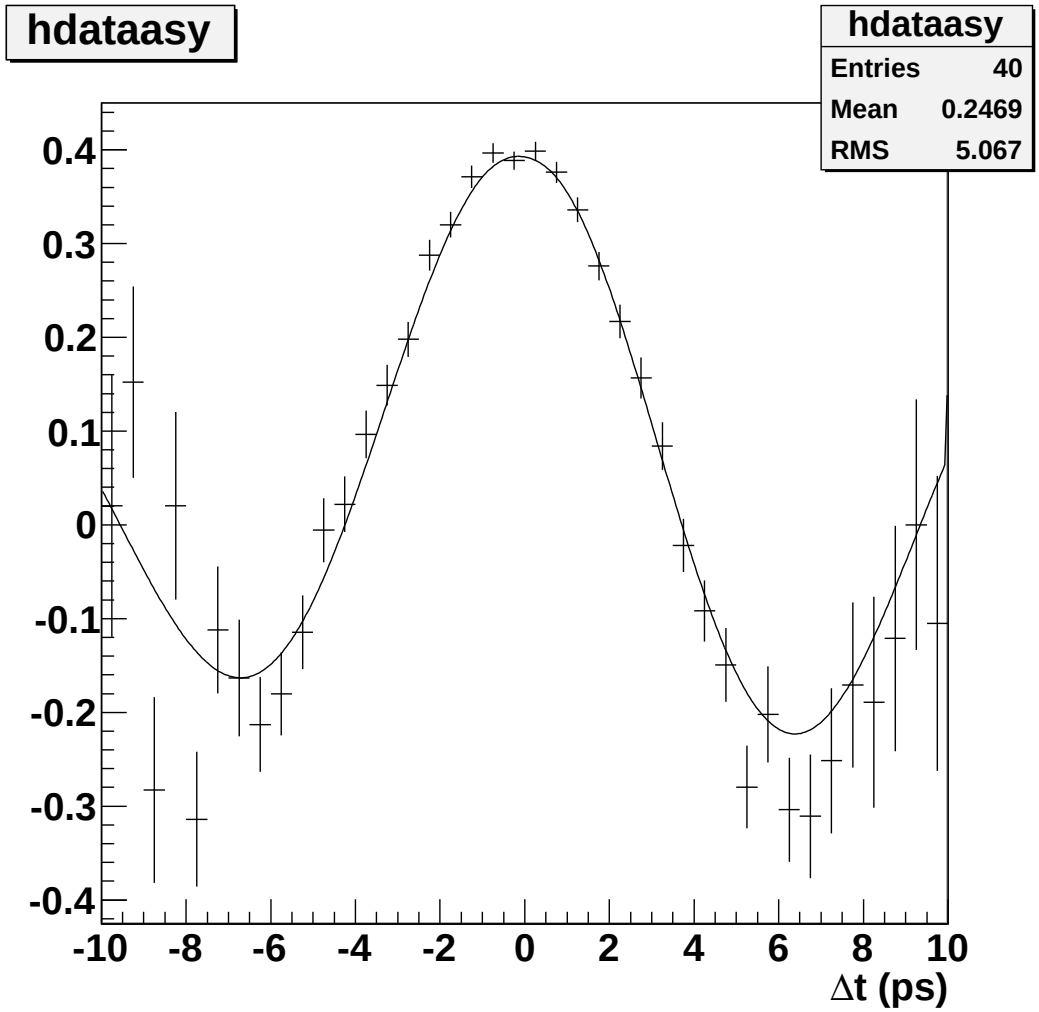

Figure 4.4: Mixing asymmetry for the data which were accumulated by Belle of SVD1+SVD2

4.5 Linearity check of $S^{\pm}$

We found that the fit procedure was the appropriate way. Then we needed to confirm that $S^{\pm}$ which were returned from the fitting program were true $S^{\pm}$. In order to check it, we generated 14 kind of signal MC and fitted them. These samples were generated with different combinations of $R = |\frac{A(DCSD)}{A(CFD)}|$, weak phase $\phi_1 + \frac{\phi_3}{2}$ and strong phase δ shown in Table 4.3. The number of generation events for each parameter sets is 6.5 million. It is $\simeq 32$ times of the expected number of the events in the data which were accumulated by Belle. Calculated $S^{\pm}$ from input parameters and the fit results also are shown in Table 4.3. We fitted these results with a linear function as shown in Figure 4.5 and Table 4.4. As you can see, there are some bias in $S^{\pm}$ fit.

Table 4.3: MC parameter set and fit results of linearity check.

R	$\phi_1 + \frac{\phi_3}{2}$	δ	input $S^{\pm}$	S^+ fit result	S^- fit result
0.05	$-\frac{\pi}{4}$	0.	0.10	0.109±0.003	0.096±0.003
0.04	$-\frac{\pi}{4}$	0.	0.08	0.086±0.003	0.071±0.003
0.0245	$-\frac{\pi}{4}$	0.	0.049	0.061±0.003	0.044±0.003
0.02	-0.89685	0.	0.039	0.040±0.003	0.034±0.003
0.02	-0.40552	0.	0.029	0.033±0.003	0.023±0.003
0.02	-0.18547	0.	0.0145	0.016±0.003	0.011±0.003
0.02	$\frac{\pi}{2}$	0.	0.0	0.010±0.003	-0.003±0.003
0.	0.89685	0.	0.0	0.006±0.003	-0.008±0.003
0.02	0.18547	0.	-0.0145	-0.006±0.003	-0.021±0.003
0.02	0.40552	0.	-0.029	-0.023±0.003	-0.032±0.003
0.02	0.89685	0.	-0.039	-0.037±0.003	-0.049±0.003
0.0245	$\frac{\pi}{4}$	0.	-0.049	-0.044±0.003	-0.056±0.003
0.04	$\frac{\pi}{4}$	0.	-0.08	-0.074±0.003	-0.088±0.003
0.05	$\frac{\pi}{4}$	0.	-0.10	-0.091±0.003	-0.104±0.003

Table 4.4: $S^{\pm}$ linearity.

	Gradient	Y-intercept
S^+	1.00±0.01	0.0060±0.0007
S^-	1.00±0.01	-0.0058±0.0007

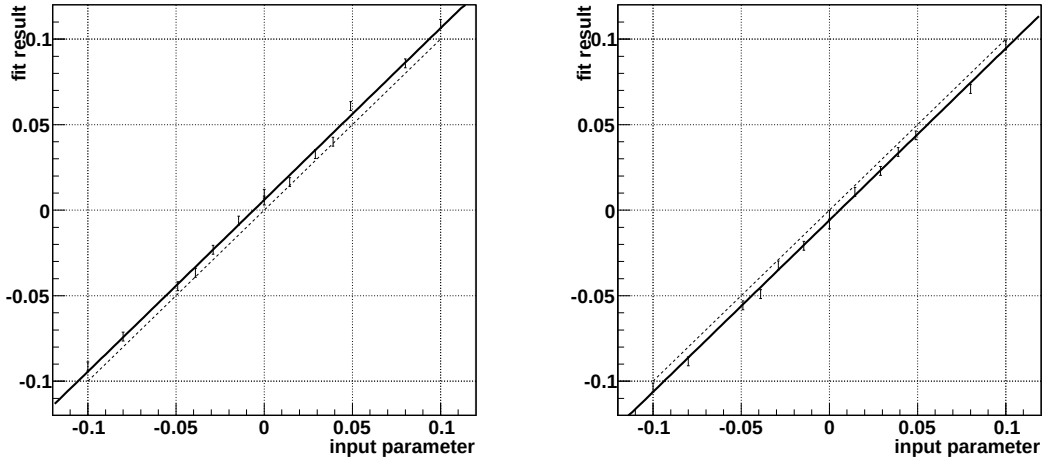

(a) S^{+} linearity

(b) S^{-} linearity

Figure 4.5: $S^{\pm}$ linearity. Solid line is fit line. Dashed line is a line of $x = y$.

4.5.1 Vertex shift bias

We studied an occasion of the bias in MC and we found that the events with wrong identification with respect to flavor caused the bias.

On investigation we found that came from non-primary effect. If non-primary particle was used as primary particle at flavor tag, flavor identification was mistaken. For example, a lepton from charm was mistaken for a lepton from bottom. And the vertex of tag-side B has bias from the flight length of the mother particle of non-primary particle.

We investigated the differences between the vertices of the events with correct identification and the events with wrong identification. Then we found that the vertices of tag-side B were different an average of $5\,\mu m$.

Figure 4.6 shows the difference between measured z and generated z of signal MC. The mean of the difference is $26\,\mu m$ for events with correct identification and $31\,\mu m$ for events with wrong identification. We checked the correlation between the bias of the vertex and y-intercept of $S^{\pm}$ linearity. We added the correction to Δz of the events with wrong identification and checked $S^{\pm}$ linearity. As shown in Figure 4.7, y-intercepts are proportional to the bias of the vertex. The result of $-4.35\,\mu m$ correction are shown in Figure 4.8 and Table 4.5. There is no bias. Thus, we concluded that the source of the bias in $S^{\pm}$ is due to mistaken flavor identification which affect vertex position.

Table 4.5: $S^{\pm}$ linearity with the bias of the vertex of the events with wrong identification.

	Gradient	Y-intercept
S^+	1.00±0.01	-0.0004±0.0007
S^-	1.00±0.01	0.0005±0.0007

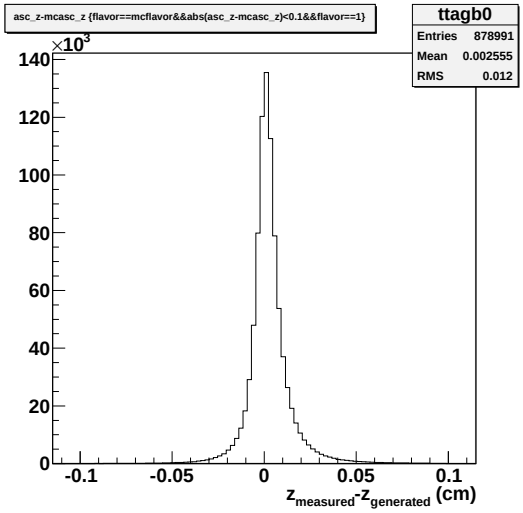

(a) true tagged B^0. mean = 25.6 μm

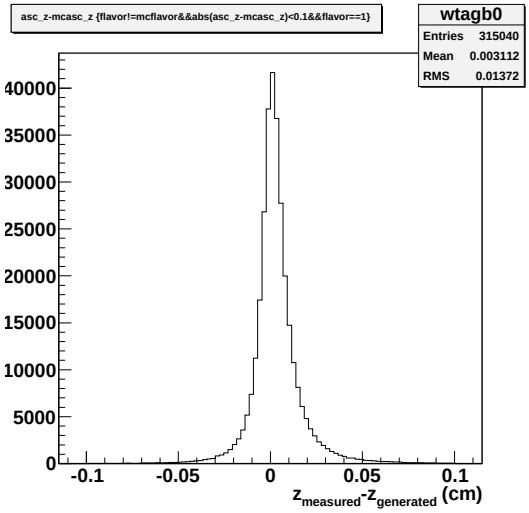

(b) wrong tagged B^0. mean = 31.1 μm

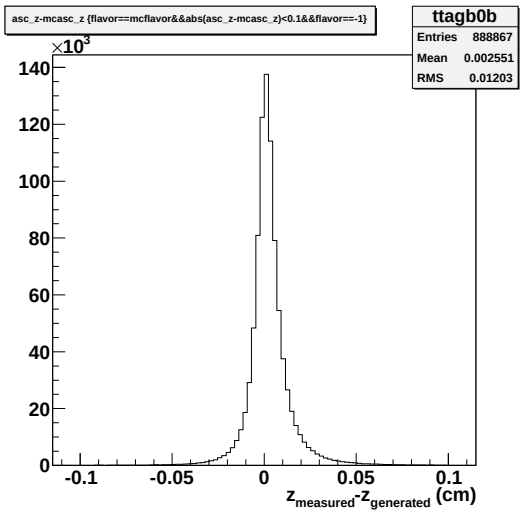

(c) true tagged $\overline{B^0}$. mean = 25.5 μm

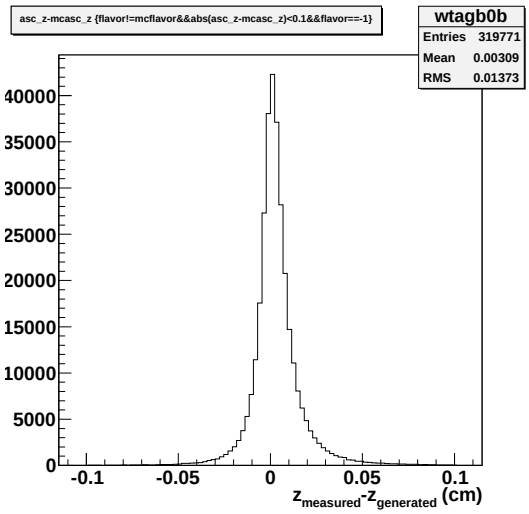

(d) wrong tagged $\overline{B^0}$. mean = 30.9 μm

Figure 4.6: Difference between measured z and generated z of signal MC (6.5 million events)

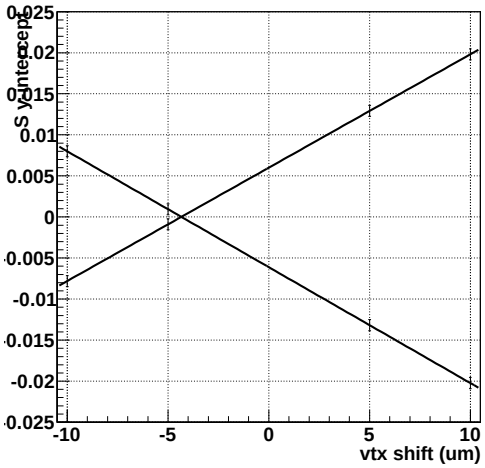

Figure 4.7: Correction of the vertex of the events with wrong identification vs. y-intercept of $S^{\pm}$ linearity. Ever-increasing line is S^+ and ever-decreasing line is S^-.

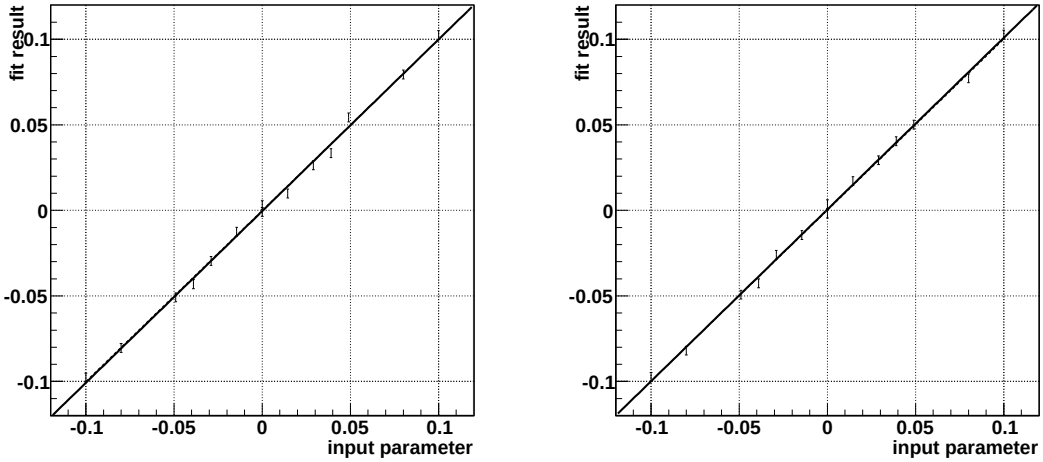

(a) S^+ linearity (b) S^- linearity

Figure 4.8: $S^{\pm}$ linearity with the bias of the vertex of the events with wrong identification.

4.5.2 Effect from tag side interference

We investigated tag side interference (TSI) effect to $S^{\pm}$ by toy-MC.

To check the influence of the bias in vertex position on tag side interference, we prepared toy-MC like $D^{*}l\nu$. We generated 2 kind of toy-MC. In order to reproduce the bias of the vertex, the vertex of the events with wrong identification were shifted from the calculated value from PDF. Other parameters were generated according to PDF. We prepared 14 kind of toy-MC samples. Then S_{tag} were fitted by the same method as $S^{\pm}$. Table 4.6 shows generation condition and fit results.

Table 4.6: $S^{\pm}_{tag}$ in toy-MC.

Generation condition		fit results	
input $S^{\pm}_{tag}$	bias of the events with wrong identification	S^{+}_{tag}	S^{-}_{tag}
0.10	0 μm	0.100±0.002	0.097±0.002
0.08	0 μm	0.081±0.002	0.079±0.002
0.049	0 μm	0.050±0.002	0.049±0.002
0.039	0 μm	0.038±0.002	0.040±0.002
0.029	0 μm	0.027±0.002	0.032±0.002
0.0145	0 μm	0.016±0.002	0.016±0.002
0.0	0 μm	0.000±0.002	0.001±0.002
0.0	0 μm	0.000±0.002	0.001±0.002
-0.0145	0 μm	-0.019±0.002	-0.011±0.002
-0.029	0 μm	-0.030±0.002	-0.029±0.002
-0.039	0 μm	-0.040±0.002	-0.039±0.002
-0.049	0 μm	-0.051±0.002	-0.046±0.002
-0.08	0 μm	-0.083±0.002	-0.078±0.002
-0.10	0 μm	-0.100±0.002	-0.102±0.002
0.10	4 μm	0.092±0.002	0.109±0.002
0.08	4 μm	0.073±0.002	0.089±0.002
0.049	4 μm	0.040±0.002	0.057±0.002
0.039	4 μm	0.030±0.002	0.048±0.002
0.029	4 μm	0.021±0.002	0.039±0.002
0.0145	4 μm	0.004±0.002	0.026±0.002
0.0	4 μm	-0.007±0.002	0.008±0.002
0.0	4 μm	-0.008±0.002	0.008±0.002
-0.0145	4 μm	-0.026±0.002	-0.006±0.002
-0.029	4 μm	-0.035±0.002	-0.023±0.002
-0.039	4 μm	-0.049±0.002	-0.031±0.002
-0.049	4 μm	-0.062±0.002	-0.040±0.002
-0.08	4 μm	-0.089±0.002	-0.073±0.002
-0.10	4 μm	-0.111±0.002	-0.090±0.002

We fitted $S^{\pm}_{tag}$ fit results with a linear function and found that the bias of vertices also makes the bias of $S^{\pm}_{tag}$ as shown in Figure 4.9.

The fit results of $S^{\pm}_{tag}$ are described as:

$$S^{+}_{tag} \rightarrow S^{+}_{tag} - \Delta S \tag{4.29}$$

$$S^{-}_{tag} \rightarrow S^{-}_{tag} + \Delta S \tag{4.30}$$

where ΔS is the S bias. As seen from above $S^{\pm}_{tag}$ are the addition of TSI and the bias which comes from the bias of vertices. Using eq.4.29, 4.30, eq.4.16 $\sim$ 4.19 are represented as:

$$S^{+}_{fav} = S^{+} + S^{-}_{tag} \tag{4.31}$$

$$S^{+}_{sup} = S^{+} - S^{+}_{tag} \tag{4.32}$$

$$S^{-}_{fav} = S^{-} + S^{+}_{tag} \tag{4.33}$$

$$S^{-}_{sup} = S^{-} - S^{-}_{tag}. \tag{4.34}$$

Then $S^{\pm}$ can be extracted even if the precise value of ΔS is unknown.

It confirmed by toy-MC that ΔS is canceled. First, to obtain $S^{\pm}_{tag}$ include ΔS, we made toy-MC like $D^* l\nu$ with the bias of the vertices. Input values for S_{tag} are $S^{+}_{tag} = -0.0096$ and $S^{-}_{tag} = 0.0067$ for the events which has no lepton in the children of tag side B (non-lepton tag events) and $S^{\pm}_{tag} = 0.$ for the other events (lepton tag events). Then fits to obtain S_{tag} were performed. Fit results of $S^{\pm}_{tag}$ for non-lepton tag are:

$$S^{+}_{tag} = -0.0223 \tag{4.35}$$

$$S^{-}_{tag} = 0.0180. \tag{4.36}$$

Fit results of $S^{\pm}_{tag}$ for lepton tag are:

$$S^{+}_{tag} = -0.0051 \tag{4.37}$$

$$S^{-}_{tag} = -0.0013. \tag{4.38}$$

Second, we made toy-MC with TSI and the bias of the vertices. Input values for $S^{\pm}$ were varied from -0.1 to 0.1. Input values for $S^{\pm}_{tag}$ are $S^{+}_{tag} = -0.0096$ and $S^{-}_{tag} = 0.0067$ for non-lepton tag events and $S^{\pm}_{tag} = 0.$ for lepton tag events. Then fits to obtain $S^{\pm}$ were performed. For $S^{\pm}_{tag}$ in fitted PDF, we used fit results of S_{tag} (eq.4.36 $\sim$ 4.38). The condition of generation and fit are in Table 4.7.

$S^{\pm}$ linearity fit results are shown in Figure 4.10. Comparison with Figure 4.5 shows that ΔS in $S^{\pm}_{tag}$ cancel ΔS in $S^{\pm}$.

By varying TSI in fitted PDF according to the error of $D^* l\nu$ fit for the data which were accumulated by Belle(Table 4.8), we estimate the systematic errors of TSI. It is smaller than estimated statistical error as shown in Table 4.9.

Table 4.7: The condition of linearity check of toy-MC with TSI

	Generation condition	Fitted PDF
$S^{\pm}$	-0.1 to 0.1	Fit parameters
S^{+}_{tag} (non-lepton tag)	-0.0096	-0.0223 (fit result of toy-MC)
S^{+}_{tag} (lepton tag)	0.0	-0.0051 (fit result of toy-MC)
S^{-}_{tag} (non-lepton tag)	0.0067	0.0180 (fit result of toy-MC)
S^{-}_{tag} (lepton tag)	0.0	-0.0013 (fit result of toy-MC)
the bias of wrong tag events	$4\,\mu m$	0

Table 4.8: The error of S_{tag}

	error
S^{+}_{tag}	$^{+0.0073}_{-0.0073}$
S^{-}_{tag}	$^{+0.0073}_{-0.0073}$
$S^{+}_{tag,\,lepton\,tag}$	$^{+0.0106}_{-0.0106}$
$S^{-}_{tag,\,lepton\,tag}$	$^{+0.0107}_{-0.0107}$

Table 4.9: Estimated systematic errors of TSI

source	$S^{\pm}$	error
S^{+}_{tag}	S^{+}	$^{+0.0024}_{-0.0038}$
	S^{-}	$^{+0.0022}_{-0.0003}$
S^{-}_{tag}	S^{+}	$^{+0.0014}_{-0.0011}$
	S^{-}	$^{+0.0024}_{-0.0037}$
$S^{+}_{tag,\,lepton\,tag}$	S^{+}	$^{+0.0025}_{-0.0038}$
	S^{-}	$^{+0.0021}_{-0.0002}$
$S^{-}_{tag,\,lepton\,tag}$	S^{+}	$^{+0.0005}_{-0.0018}$
	S^{-}	$^{+0.0041}_{-0.0022}$

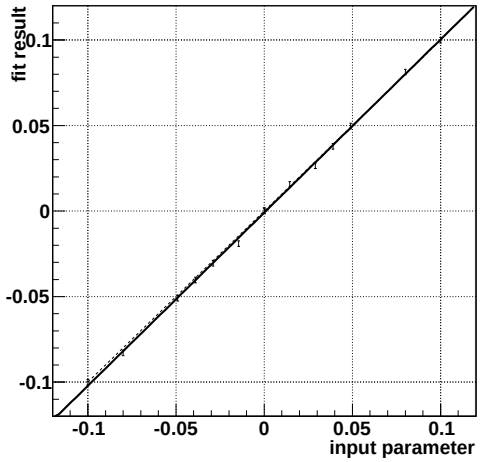

(a) S^+_{tag} generate without the bias of vertex position. $Gradient = 1.012 \pm 0.008$, $Yintercept = -0.0009 \pm 0.0004$

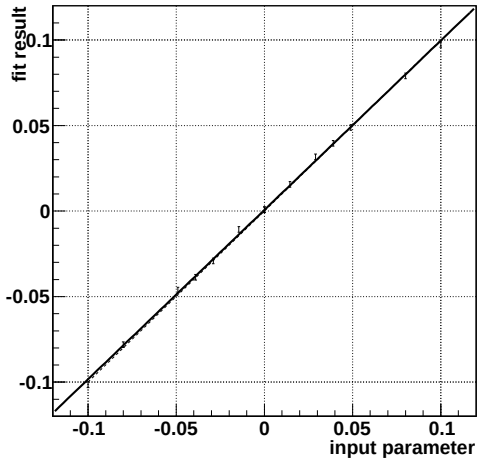

(b) S^-_{tag} generate without the bias of vertex position. $Gradient = 0.990 \pm 0.008$, $Yintercept = 0.0007 \pm 0.0004$

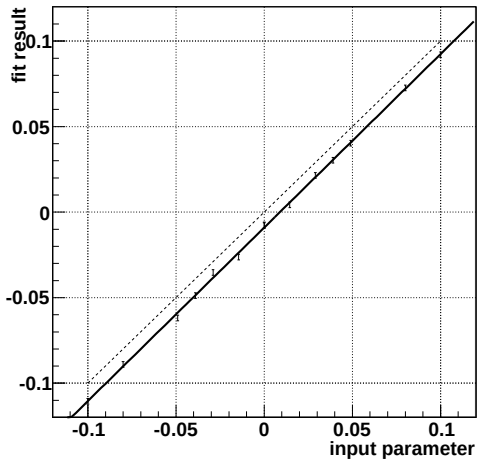

(c) S^+_{tag} generate with the bias of vertex position. $Gradient = 1.014 \pm 0.008$, $Yintercept = -0.0090 \pm 0.0004$

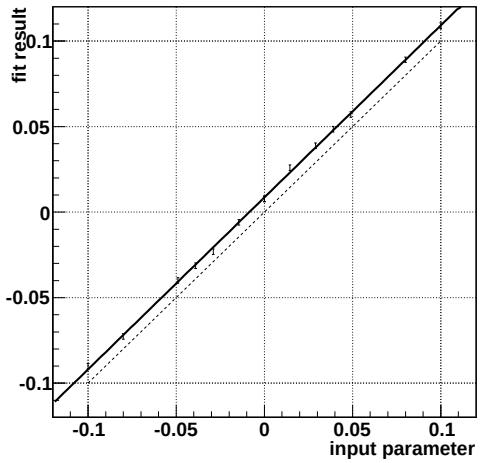

(d) S^-_{tag} generate with the bias of vertex position. $Gradient = 1.005 \pm 0.008$, $Yintercept = 0.0086 \pm 0.0004$

Figure 4.9: $S^{\pm}_{tag}$ linearity.

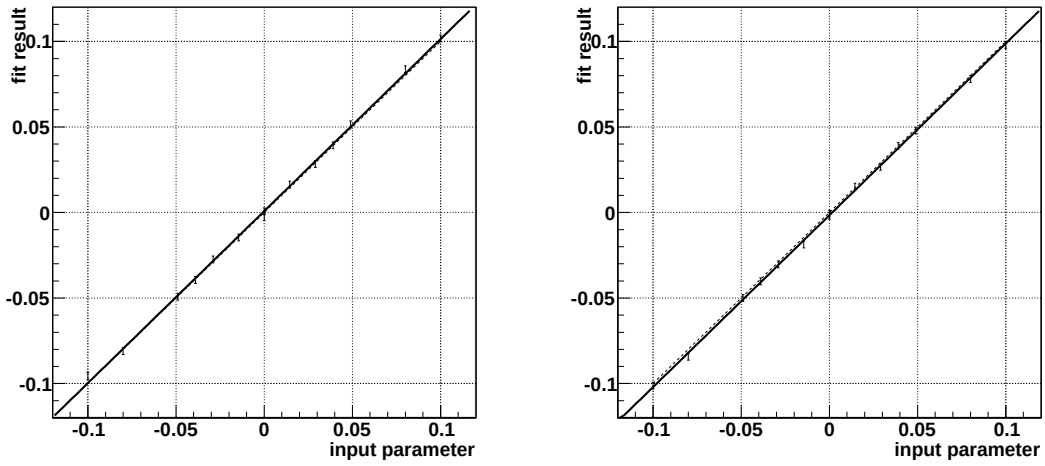

(a) S^{+} generate with the bias of vertex and TSI. $Gradient = 1.01 \pm 0.01$, $Yintercept = 0.0008 \pm 0.0005$

(b) S^{-} generate with the bias of vertex and TSI. $Gradient = 1.00 \pm 0.01$, $Yintercept = -0.0016 \pm 0.0005$

Figure 4.10: $S^{\pm}$ linearity with TSI.

We also changed fit parameters $S^{\pm}$ to a and c and estimated systematic errors. This parameterization are used at babar and described as:

$$a = -\frac{(S^+ + S^-)}{2} \tag{4.39}$$

$$c = -\frac{(S^+ - S^-)}{2}. \tag{4.40}$$

Table 4.10 is fit result for a toy-MC sample that of input parameters are $a = -0.039$ and $c = 0$.

Table 4.10: Fit parameters a and c fit results

	a		c	
input	-0.039		0.0	
	0.0396±0.0014		0.0004±0.0014	
systematic error source	difference		difference	
S^+_{tag} +1 σ	0.0387±0.0014	-0.0009	-0.0017±0.0014	-0.0021
S^+_{tag} -1 σ	0.0405±0.0014	+0.0009	0.0026±0.0014	+0.0022
S^-_{tag} +1 σ	0.0387±0.0014	-0.0009	0.0026±0.0014	+0.0022
S^-_{tag} -1 σ	0.0405±0.0014	+0.0009	-0.0017±0.0014	-0.0021
$S^+_{tag,\,lepton\,tag}$ +1 σ	0.0386±0.0014	-0.0010	-0.0017±0.0014	-0.0021
$S^+_{tag,\,lepton\,tag}$ -1 σ	0.0406±0.0014	+0.0010	0.0026±0.0014	+0.0022
$S^-_{tag,\,lepton\,tag}$ +1 σ	0.0386±0.0014	-0.0010	0.0026±0.0014	+0.0022
$S^-_{tag,\,lepton\,tag}$ -1 σ	0.0406±0.0014	+0.0010	-0.0017±0.0014	-0.0021

4.6 Extraction of $S^{\pm}$

We fitted the CP violating parameters $S^{\pm}$ using the data which were accumulated by Belle. The PDF include S_{tag} are given as:

$$P(q=-1; B_{sig}\to D^{*\mp}\pi^{\pm}) = (1-w_{\overline{B^0}})P(B^0\to D^{*\mp}\pi^{\pm}) + w_{B^0}P(\overline{B^0}\to D^{*\mp}\pi^{\pm}) \quad (4.41)$$

$$P(q=+1; B_{sig}\to D^{*\pm}\pi^{\mp}) = (1-w_{B^0})P(\overline{B^0}\to D^{*\pm}\pi^{\mp}) + w_{\overline{B^0}}P(B^0\to D^{*\pm}\pi^{\mp}) \quad (4.42)$$

$$P(B^0\to D^{*-}\pi^{+}) = \frac{e^{-\frac{|\Delta t|}{\tau_{B^0}}}}{8\tau_{B^0}}[1 + C\cos(\Delta m\Delta t) - (S^{-} + S^{+}_{tag})\sin(\Delta m\Delta t)] \quad (4.43)$$

$$P(B^0\to D^{*+}\pi^{-}) = \frac{e^{-\frac{|\Delta t|}{\tau_{B^0}}}}{8\tau_{B^0}}[1 - C\cos(\Delta m\Delta t) - (S^{+} - S^{+}_{tag})\sin(\Delta m\Delta t)] \quad (4.44)$$

$$P(\overline{B}^0\to D^{*+}\pi^{-}) = \frac{e^{-\frac{|\Delta t|}{\tau_{B^0}}}}{8\tau_{B^0}}[1 + C\cos(\Delta m\Delta t) + (S^{+} + S^{-}_{tag})\sin(\Delta m\Delta t)] \quad (4.45)$$

$$P(\overline{B}^0\to D^{*-}\pi^{+}) = \frac{e^{-\frac{|\Delta t|}{\tau_{B^0}}}}{8\tau_{B^0}}[1 - C\cos(\Delta m\Delta t) + (S^{-} - S^{-}_{tag})\sin(\Delta m\Delta t)] \quad (4.46)$$

where w_{B^0} and $w_{\overline{B^0}}$ are the probability of wrong identification with respect to B^0 and $\overline{B^0}$, respectively. Because measured S_{tag} are include ΔS, we used $S^{\pm}_{tag}$ which are measured from $D^*l\nu$ sample with lepton tag events for $D^*\pi$ events with lepton tag. S_{tag} are shown in Table 4.11.

Table 4.11: S_{tag} which are measured from $D^*l\nu$ sample

S^{+}_{tag} (non-lepton tag events)	-0.0096±0.0073
S^{-}_{tag} (non-lepton tag events)	+0.0067±0.0073
S^{+}_{tag} (lepton tag events)	-0.0192±0.0106
S^{-}_{tag} (lepton tag events)	+0.0103±0.0106

The fit results are:

$$S^{+} = 0.000\pm0.017 \quad (4.47)$$

$$S^{-} = 0.057\pm0.017 \quad (4.48)$$

where the error is statistical error. Distributions of Δt are shown in Fig.4.11.

The asymmetry plots using all events and the good quality flavor tagging ($0.75 < |r| < 1.0$) events are shown in Fig.4.12 and Fig.4.13, respectively.

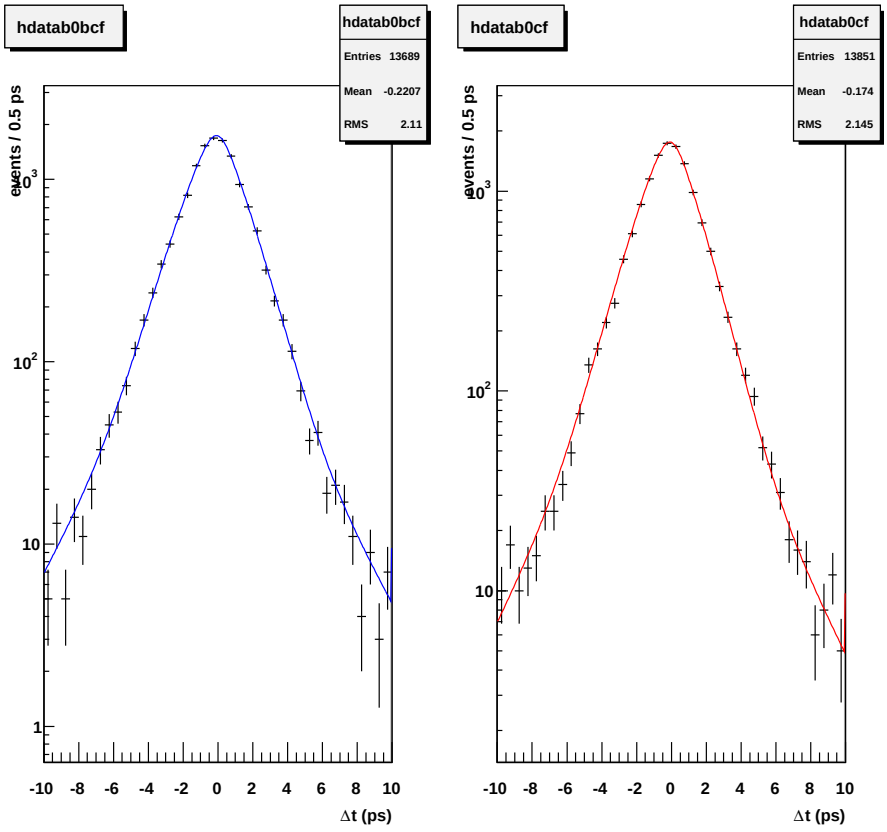

(a) Δt plot for favored mode. Left plot is $B_{tag} = B^0$ events and right plot is $B_{tag} = \overline{B^0}$ events.

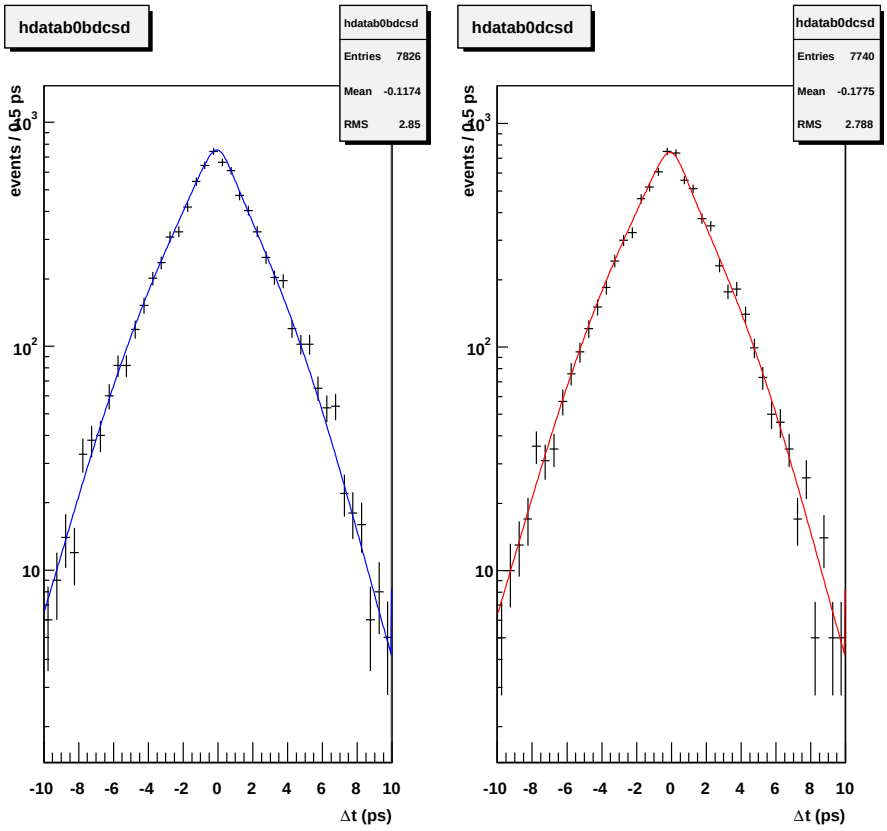

(b) Δt plot for suppressed mode. Left plot is $B_{tag} = B^0$ events and right plot is $B_{tag} = \overline{B^0}$ events.

Figure 4.11: Δt plot

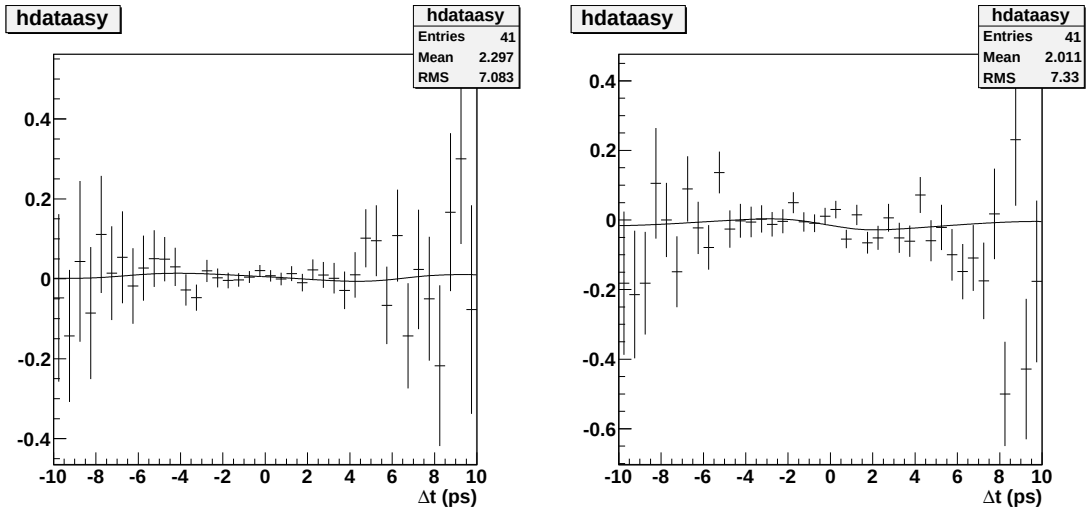

(a) asymmetry plot for favored mode (b) asymmetry plot for suppressed mode

Figure 4.12: Asymmetry plots using all events

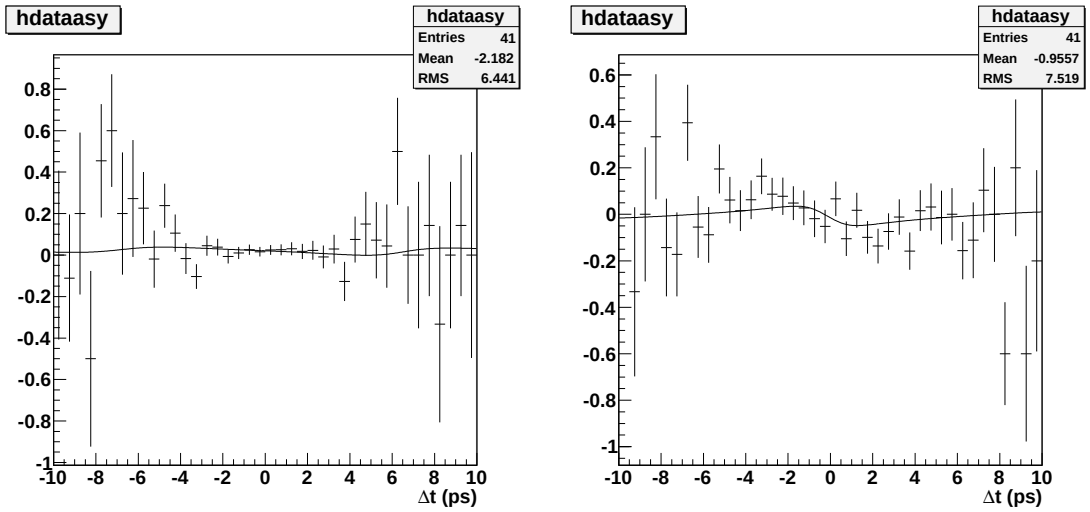

(a) asymmetry plot for favored mode (b) asymmetry plot for suppressed mode

Figure 4.13: Asymmetry plots using the good quality flavor tagging ($0.75 < |r| < 1.0$) events

4.7 Systematic error

The systematic errors come from the uncertainties of parameters that are fixed in the fit. For estimating contributions from the uncertainties to the fit results, we repeated the fit by varying each parameter by a certain amount, and assigned systematic errors at differences from nominal fit results. The source of systematic errors that has correlation between S^+ and S^- are listed.

- Δt resolution
  The parameters, f, s, σ, τ are the sources and shown in chapter.4.

- background Δt shape

  The parameters in Table.4.1 were varied by $\pm 1\sigma$.

- signal fraction

  The signal/background fraction were varied by $\pm 1\sigma$.

- wrong tag fraction

  The w and Δw in Table.3.6 were varied by $\pm 1\sigma$.

- vertexing

  We changed the cut and repeated the $S^{\pm}$ fit. The cuts are listed in Table 4.12.

Table 4.12: Value of vertexing cut

parameters	default	changed value
Vertex fit quality	h < 50	20, 100
Track selection for multi-track vertex	$\sigma_z < 200\,\mu m$	no-cut
Track selection for single-track vertex	$\sigma_z < 500\,\mu m$	no-cut
Realistic lifetime	$\lvert\Delta t\rvert < 70\,ps$	$40\,ps,\ 100\,ps$

- physics parameters (τ_{B^0}, Δm)

  We changed according to PDG error.

- tag-side interference

  We changed according to the measurement of $D^* l\nu$.

Although it is expected that there are some CP violating background, neutral B background is almost negligible. Therefore systematic error from CP violating background can be ignored.

Total systematic error is ± 0.011 for both S^+ and S^-. Table.4.13 summarizes the systematic errors. The error of previous analysis is ± 0.014 for both S^+ and S^- as shown in Table.4.13. In this analysis, we found the occasion of $S^{\pm}$ fit bias. The bias was included in tag-side interference and their systematic errors were combined.

Table 4.13: Systematic error

Sources	S^+	S^-	previous analysis
Δt resolution	+0.010 -0.010	+0.010 -0.010	±0.005
background Δt shape	+0.0001 -0.0001	+0.0001 -0.0001	±0.0001
signal fraction	+0.0010 -0.0005	+0.0007 -0.0007	±0.002
wrong tag fraction	+0.0006 -0.0005	+0.0005 -0.0004	±0.002
vertexing	+0.0008 -0.0001	+0.0004 -0.0005	±0.004
physics parameters (τ_{B^0}, Δm)	+0.0001 -0.0001	+0.0007 -0.0005	±0.001
tag-side interference	+0.005 -0.005	+0.005 -0.006	±0.005
$S^{\pm}$ fit bias			±0.010
combined	+0.011 -0.011	+0.011 -0.011	±0.014

Chapter 5

Conclusion

5.1 Result

The results of this analysis are

$$S^+ \;=\; -\frac{2R}{1+R^2}\sin\left(2\phi_1+\phi_3+\delta\right) \;=\; 0.000\pm0.017\pm0.011 \tag{5.1}$$

$$S^- \;=\; -\frac{2R}{1+R^2}\sin\left(2\phi_1+\phi_3-\delta\right) \;=\; 0.057\pm0.017\pm0.011 \tag{5.2}$$

where the first error is statistical and the second error is systematic. These results are shown in Figure.5.1. The vertical axis is S^- and the horizontal axis is S^+. In this plot, we ignored the difference of detection efficiency that originated from charge conjugate. The shaded regions indicate allowed regions. The darkened circled regions displays $1\,\sigma$, $2\,\sigma$ and $3\,\sigma$ uncertainties.

We can also express the results as parameters a, c:

$$a \;=\; \frac{2R}{1+R^2}\sin\left(2\phi_1+\phi_3\right)\cos\delta \;=\; -\frac{(S^+ + S^-)}{2} \;=\; -\,0.029\pm0.012\pm0.011 \tag{5.3}$$

$$c \;=\; \frac{2R}{1+R^2}\cos\left(2\phi_1+\phi_3\right)\sin\delta \;=\; -\frac{(S^+ - S^-)}{2} \;=\; 0.029\pm0.012\pm0.011. \tag{5.4}$$

Since a is the amplitude of the asymmetry distribution, the deviation of a from zero is the significance of CP violation. We obtained that the significance was 2.0σ. While the deviation of $c \propto \cos\left(2\phi_1+\phi_3\right)\sin\delta$ from zero means the possibility that δ has some value. Figure.5.2 shows the comparison with previous results of the Belle and the Babar.

The next step for the analysis of $B^0\overline{B}^0 \to D^{*\mp}\pi^{\pm}$ is the constraint on $(2\phi_1+\phi_3)$. We have two measurements, S^+ and S^-, while they include three unknowns, $(2\phi_1+\phi_3)$, R and δ. It can be calculated by the following procedure:

1. δ is assumed to be a value that consists with the theoretical value and the measurement value.

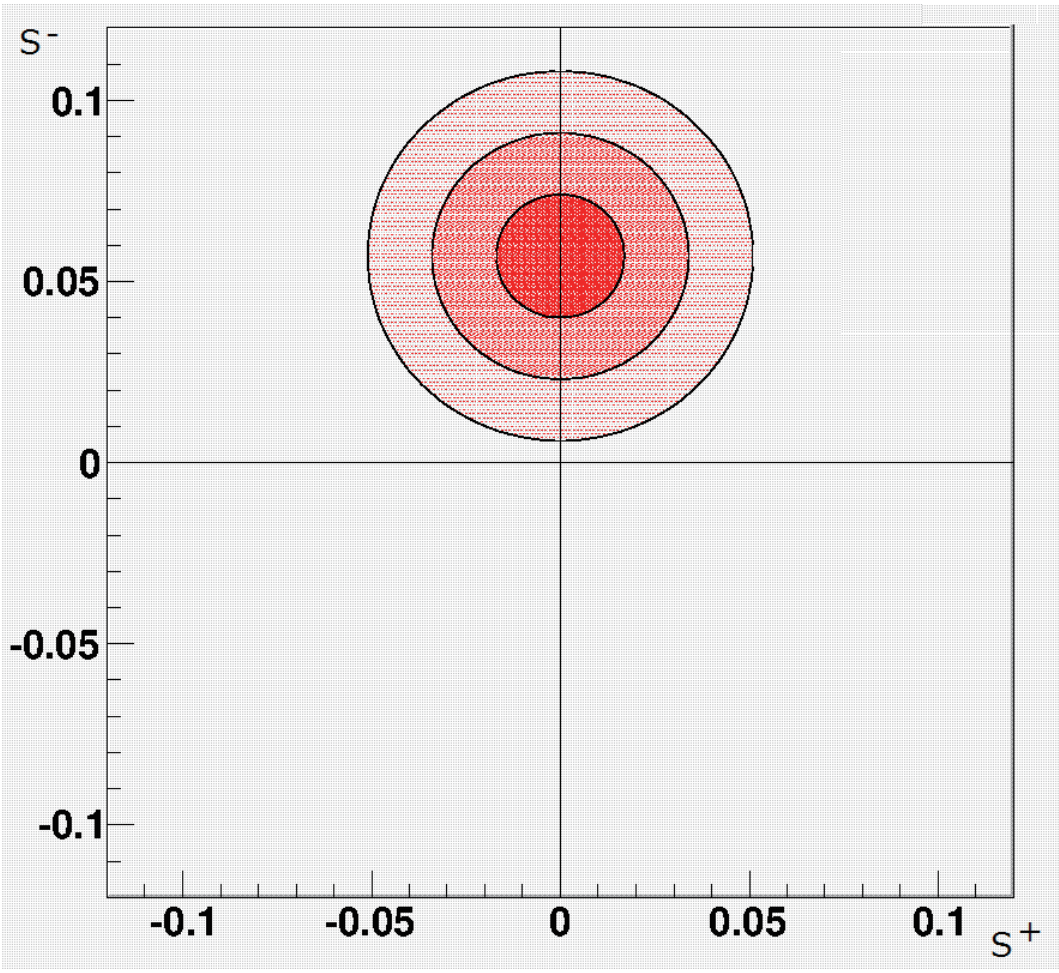

Figure 5.1: Result of the $S^{\pm}$ measurements. The vertical axis is S^{-} and the horizontal axis is S^{+}.

2. We fix δ and generate many parameterized MC experiments with the same sensitivity as the data sample. Parameters are $(2\phi_1 + \phi_3)$ and R.

3. We compare observed a, c from MC with measured a, c. Then we get the confidence level for each MC parameters.

In addition, R can be estimated by following equation:

$$R = \sqrt{\frac{\mathcal{B}(B^0 \to D_s^{*+}\pi^-)}{\mathcal{B}(B^0 \to D^{*-}\pi^+)}} \frac{f_{D^*}}{f_{D_s^*}} \tan\theta_C. \tag{5.5}$$

Using it, the parameter of MC can be reduced only to $(2\phi_1 + \phi_3)$.

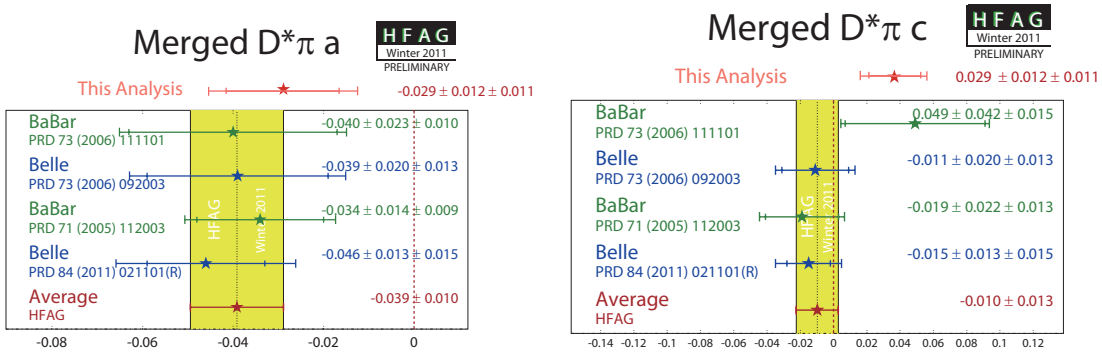

(a) a parameter (b) c parameter

Figure 5.2: comparison with the previous results of the Belle and the Babar

Bibliography

[1] A. D. Sakharov, JETP Letters **5**, 24 (1967).

[2] N. Cabibbo, Phys. Rev. Lett. **10**, 531 (1963).

[3] M. Kobayashi and T. Maskawa, Prog. Theo. Phys. **49**, 652 (1973).

[4] L. Wolfenstein, Phys. Rev. Lett. **51**, 1945 (1983).

[5] K. Abe *et al.* (Belle Collaboration), Phys. Rev. D **66** (2002) 071102(R).

[6] *et al.* (Babar Collaboration), Phys. Rev. Lett. **89** (2002) 201802.

[7] I. Dunietz and R. G. Sachs, Phys. Rev. D **37** (1988) 3186, *Erratim*: Phys. Rev. D **39** (1989) 3515.

[8] I. Dunietz, Phys. Lett. B **427** (1998) 179.

[9] S. Kurokawa and E. Kikutani, Nucl. Instrum. Methods Phys. Res., Sect. A **499**, 1 (2003).

[10] Belle Collaboration, A. Abashian *et al.*, Nucl. Instrum. Methods Phys. Res., Sect. A **479**, 117 (2002).

[11] G. Alimonti *et al.*, Nucl. Instrum. Methods Phys. Res., Sect. A **453**, 71 (2000).

[12] Y. Ushiroda, Nucl. Instrum. Methods Phys. Res., Sect. A **511**, 6 (2003).

[13] H. Hirano *et al.*, Nucl. Instrum. Methods Phys. Res., Sect. A **455**, 294 (2000).

[14] T. Iijima *et al.*, Nucl. Instrum. Methods Phys. Res., Sect. A **453**, 321 (2000).

[15] H. Kichimi *et al.*, Nucl. Instrum. Methods Phys. Res., Sect. A **453**, 315 (2000).

[16] H. Ikeda *et al.*, Nucl. Instrum. Methods Phys. Res., Sect. A **441**, 401 (2000).

[17] A. Abashian *et al.*, Nucl. Instrum. Methods Phys. Res., Sect. A **449**, 112 (2000).

[18] R. Santonico and R. Cardarelli, Nucl. Instrum. Methods Phys. Res., Sect. A **187**, 377 (1981).

[19] D. J. Lange, Nucl. Instrum. Methods Phys. Res., Sect. A **462**, 152 (2001).

[20] H. Tajima, H. Aihara, T. Higuchi *et al.*. arXiv:hep-ex/0301026

[21] K. Abe, *et al.* (Belle Collaboration), Phys. Rev. Lett. **88** (2002) 171801.

[22] O. Long, M. Baak, R. N. Cahn and D. Kirkby, hep-ex/0303030.

[23] Kazutaka Sumisawa , Belle Analysis School, The road towards final sin2phi1 (2) , (2012).

[24] K. Hara, M. Hazumi *et al.* (Belle Collaboration), Phys. Rev. Lett. **89** (2002) 251803

[25] J. Beringer *et al.* (Particle Data Group), PR **D86**, 010001 (2012).

[26] F. J. Ronga, T. R. Sarangi *et al.* (Belle Collaboration), Phys. Rev. D **73** (2006) 092003.